Single-molecule mitochondrial DNA imaging reveals heteroplasmy dynamics shaped by developmental bottlenecks and selection in different organs *in vivo*

Rajini Chandrasegaram[1,2], Sara Gottardo[1*], Abhilesh Dhawanjewar[1,2*], Antony M. Hynes-Allen[1,2*], Beitong Gao[1,2,3], Suvagata Roy Chowdhury[1], Luis Carlos Tábara[1,4], Michele Frison[1,2], Stavroula Petridi[1,2], Patrick F. Chinnery[1,2], Julien Prudent[1], Hansong Ma[5], Jelle van den Ameele[1,2**]

[1] MRC Mitochondrial Biology Unit and [2] Department of Clinical Neurosciences, University of Cambridge, UK

[3] Department of Genetics, University of Cambridge, UK

[4] Present address: Centre for Genomic Regulation (CRG), The Barcelona Institute of Science and Technology, Barcelona, Spain

[5] School of Biosciences, University of Birmingham, B15 2TT, UK

* Equal contribution

** Correspondence to jv361@cam.ac.uk

Abstract

Mitochondrial DNA (mtDNA) exists in many copies per cell, with cell-to-cell variability in mutation load, known as heteroplasmy. Developmental and age-related expansion of pathogenic mtDNA mutations contributes to mitochondrial and neurodegenerative disease pathogenesis. Here, we describe an approach for *in situ* sequence-specific detection of single mtDNA molecules (mtDNA-smFISH). We apply this method to visualize and measure *in situ* mtDNA and heteroplasmy levels at single-cell resolution in whole-mount *Drosophila* tissue and cultured human cells. In *Drosophila*, we identify a somatic mtDNA bottleneck during neurogenesis. This amplifies heteroplasmy variability between neurons, as predicted from a mathematical bottleneck model, predisposing individual neurons to a high mutation load. However, both during neurogenesis and oogenesis, mtDNA segregation is accompanied by purifying selection, promoting wild-type over pathogenic mtDNA. mtDNA-smFISH thus elucidates novel mechanisms whereby developmental cell-fate transitions, accompanied by changes in cell morphology, behaviour and metabolism, will shape disease-relevant and tissue-specific transmission and selection of mtDNA mutations.

Keywords

Mitochondrial DNA, heteroplasmy, single-molecule fluorescent *in situ* hybridisation, bottleneck, purifying selection, mitochondrial disease.

Introduction

Unlike the nuclear genome, which is haploid or diploid in most animal cells, the mitochondrial genome (mtDNA) occurs in up to many thousands of copies per cell. Most human cells carry a mixture of wild-type (WT) and mutated mtDNA (heteroplasmy) [1-6], with considerable cell-to-cell variability in mutation load [7,8]. During development and ageing, mtDNA mutations can clonally expand to high levels in single cells, causing defects in energy production and metabolism, and eventually cell death [5,9-11]. Expansion of pathogenic mtDNA mutations follows striking tissue- and cell-type-specific patterns during development and aging [10,12], and is the main cause of inherited and sporadic adult-onset mitochondrial diseases [13]. Clonal amplification of mtDNA mutations has also been implicated in common neurodegenerative disorders like Alzheimer's and Parkinson's disease [14,15], or in cancer, where certain somatic mtDNA variants reach homoplasmy due to positive selection [16]. In *Drosophila*, deleterious mtDNA mutations have also been shown to increase within individual flies over time [17-19], contributing to developmental and aging phenotypes, and even lethality [19-25].

Variability in heteroplasmy levels between cells within a tissue, or between a mother and her offspring, can be caused by vegetative segregation. This process is driven by stochastic mechanisms, primarily the random partitioning of mtDNA during cell division and turnover of mtDNA molecules, due to the ongoing destruction and replication of mtDNA, independent of the cell cycle (relaxed replication) [7,9]. These processes lead to heteroplasmy drift, and may be modulated by purifying selection or selfish propagation, resulting respectively in a decrease or an increase of deleterious mtDNA heteroplasmy levels [6,11,18]. A special example occurs between mothers and their offspring, where heteroplasmy shifts are further accentuated by a genetic mtDNA bottleneck, due to drastic mtDNA copy number (CN) reduction in single cells during maternal germline development [26-31]. Although well studied in the germline, little is known about segregation of heteroplasmy in somatic tissues during development and aging, apart from observations from mtDNA analysis in hair follicles [32-34]. Nonetheless, this is likely to play a crucial role in determining mutational burden during life across tissues. For example, many developmental and homeostatic cell-fate transitions are accompanied by profound changes in cell volume, morphology, and metabolism, but it remains unknown how these affect the mtDNA, and may amplify shifts in heteroplasmy levels.

Current explanations of heteroplasmy shifts are mainly based on modelling of data from whole-tissue analysis [35] or single-cell sequencing and genotyping of isolated cells outside their *in vivo* context [7,8,32,36-38]. A major limitation of these approaches is that they mostly rely on tissue dissociation, losing spatial information and limiting analysis of subcellular mechanisms.

Here, we develop and validate a novel approach for *in situ* visualization of heteroplasmic mtDNA variants (mtDNA-smFISH) based on single-molecule *in situ* hybridisation (smFISH) combined with

enzyme-free hybridisation chain reaction (HCR) for signal amplification. We apply this method to detect mtDNA heteroplasmy *in situ* in whole-mount tissue of an established *Drosophila* model of stable heteroplasmy, and in cultured human cybrid cells carrying a heteroplasmic single large-scale mtDNA deletion. In *Drosophila*, mtDNA-smFISH confirmed the presence of purifying selection against pathogenic mtDNA during oocyte development. In addition, we provide evidence for the existence of a somatic bottleneck during neurogenesis in the developing larval brain. This amplifies cell-to-cell variability in heteroplasmy levels between different progeny derived from the same neural stem cell (NSC), thus predisposing subsets of neurons and glia to high levels of deleterious mtDNA mutations, leading to mitochondrial dysfunction and disease.

Design

Current mtDNA imaging methods either lack the resolution to distinguish single mtDNA molecules [39,40], have low sensitivity [17,41], depend on mtDNA replication [42], rely on cell-penetration of enzymes and have not been used on whole-mount tissues [43,44], or are not compatible with the genetics of multicellular organisms [45]. Development of *in vivo* models and tools to measure, track and modulate heteroplasmy in somatic tissues is required to understand the cellular and molecular processes that cause somatic heteroplasmy variation and tissue-specific phenotypes of mitochondrial disease, and answer long-standing questions in the field of mitochondrial/mtDNA biology [46].

In order to develop an approach for *in situ* detection of heteroplasmic mtDNA variation in whole-mount tissues, we took advantage of recent advances in single-molecule Fluorescent *In situ* Hybridisation (smFISH) combined with Hybridisation Chain Reaction (HCR). smFISH-HCR is a well-established technique for the detection of mRNA in whole-mount tissues [47-50]. It combines short single-stranded DNA probes complementary to target nucleotide sequences with enzyme-free signal amplification based on fluorescently labelled metastable DNA hairpins (**Figure 1A)**. Third-generation smFISH-HCR achieves high signal-to-background ratios by relying on pairs of short (25bp) single-stranded DNA probes that together recognize a 52bp mRNA target sequence, and initiate HCR only when bound in close proximity and correct orientation [47] (**Figure 1B**). This allows *in situ* single-molecule detection with as few as 5 probe pairs or less [50]. In order to detect mtDNA instead of mRNA, we established a protocol of dsDNA denaturation in whole-mount tissue through heating of formaldehyde- and methanol-fixed tissue to 95ºC in 70% formamide (see methods). This allows double-stranded mtDNA to become single-stranded, enabling the probes to anneal to their complementary mtDNA-sequence *in situ,* subsequently illuminating this specific DNA region, which is monitored by fluorescence microscopy.

Results

Single-molecule Fluorescent *In Situ* Hybridisation of mtDNA (mtDNA-smFISH)

We first designed sets of 12 and 10 probe pairs to specifically detect human or *Drosophila* mtDNA respectively (**Figure S1A,B**; **Table S1**). We used these to conduct mtDNA-smFISH on human or *Drosophila melanogaster* cells cultured *in vitro*. Each probe set generated a distinct cytoplasmic punctate staining pattern in the cells of its corresponding species (human or *Drosophila*) (**Figure 1C-J**). In contrast, when the same probe sets were applied to the converse cell types (i.e. human probes on *Drosophila* cells and vice versa) no signal was detected (**Figure 1D,F**).

We next quantified signal intensity of the human probe set in Rho^0-cells (derived from ΔH2.1 cell lines carrying a 7.5kb mtDNA deletion, see methods), after ddC-mediated depletion of mtDNA (**Figure 1K-Q; S2A-M**). The mtDNA-smFISH signal-intensity showed cell-to-cell variability in the Rho^0 cell cultures upon ddC treatment (**Figure S2I,K-M**), corroborating the capacity of the method to monitor single-cell mtDNA levels. Signal-intensity compared to non-treated cells decreased progressively with continuous ddC treatment (**Figure S2I**), to reach levels that were only slightly higher than the background signal obtained from mtDNA-smFISH conducted with amplifiers only (i.e. without any probes) (**Figure 1Q; S2I,J**). In contrast, RNAse treatment before hybridization did not prevent the mtDNA-smFISH staining (**Figure S2N-Q**), all together indicating specificity of the probes for mtDNA.

To further confirm that the punctate pattern did correspond to mtDNA, we conducted fluorescent immunohistochemistry (IHC) with antibodies against mitochondrial epitopes that withstand the harsh denaturation conditions of mtDNA-smFISH. Co-IHC of ATP-synthase (**Figure 1I,J**), localised at the inner mitochondrial membrane, or of the outer mitochondrial membrane protein TOMM20 (**Figure 1K-P**), together with mtDNA-smFISH showed a clear overlay of smFISH puncta with the overall mitochondrial network, both in human and *Drosophila* cells. A gap in the ATP-synthase staining was sometimes observed at the site of mtDNA-smFISH by Airyscan super-resolution microscopy (**Figure S2R-V**). This may be due to steric hindrance from the HCR hairpins, preventing efficient antibody-access [51,52]. However, a similar lack of overlap between ATP-synthase IHC and mtDNA nucleoids has been described previously using other approaches [53-55], suggesting that mtDNA nucleoids may be situated away from mitochondrial cristae or the ATP-synthase complex within those cristae. Finally, mtDNA-smFISH combined with IHC of the nucleoid-associated mitochondrial transcription factor A (TFAM)[56-58], showed colocalization of TFAM with 78.9%±9.4 (mean±sd) of mitochondrial-localised mtDNA-smFISH puncta (**Figure 1R-V**), further indicating selective mtDNA detection. The lack of complete overlap is likely due to variability in TFAM-binding and nucleoid organization, in line with recent results from long-read single-molecule accessibility mapping[57,58].

mtDNA-smFISH in whole-mount tissue

We next applied mtDNA-smFISH to whole-mount *Drosophila* larval brains and observed a similar cytoplasmic punctate staining pattern throughout the entire brain (**Figure 2A,B**). No signal was observed in conditions without probes or amplifiers (**Figure S3A-F**), and probes recognized mtDNA from either *Drosophila yakuba* (Dyak) or *Drosophila melanogaster* (Dmel) strains, as they were designed against conserved regions of the two mitochondrial genotypes (**Figure S1;S3G-I**). To estimate sensitivity, we quantified smFISH puncta in single NSCs, which can be identified within the larval ventral nerve cord (VNC) by their large nuclear size and expression of GFP under control of a NSC-specific GAL4 [59,60]. Quantification was done in 3D in z-stacks across individual NSCs and compared to mtDNA copy number (CN) quantification by single-cell digital droplet PCR (ddPCR) of FACS-sorted nuclear GFP-labelled NSCs (**Figure S4;S5**). The average NSC mtDNA CN detected by smFISH was 246.1±47.4 (mean±sd) (**Figure 2C**), and 259.6±76.1 (mean±sd) by ddPCR (**Figure 2D**), indicating >90% efficiency of mtDNA-smFISH to detect mitochondrial nucleoids across experiments. The difference between both techniques may reflect mtDNA replication occurring in some nucleoids, which are therefore expected to have >1 copy of mtDNA per mtDNA-smFISH punctum [58]. Importantly, these quantifications indicate that also *in vivo*, and in non-mammalian species, the majority of nucleoids harbor only a single copy of mtDNA, in line with previous observations from *in vitro* studies with cultured mammalian cells [58,61].

Expression of a mitochondrial-targeted restriction enzyme, mito-XhoI in *Drosophila* cells was previously shown to linearise mtDNA through digestion at a single restriction site (**Figure 2E**), resulting in mtDNA degradation and depletion [62]. When we expressed mito-XhoI specifically in NSCs and their progeny with *Worniu*-GAL4, the mtDNA-smFISH signal was significantly reduced (**Figure 2F-H**), similar to what was observed for the human probe set in mtDNA-depleted Rho^0-cells (**Figure 1K-Q**). Only glial cells and NSC-lineages not expressing *Worniu*-GAL4 retained mtDNA-smFISH signal (**Figure 2F,H**).

Co-IHC of a mitochondrial-targeted Flag-tagged transgene expressed in NSCs showed overlap with mtDNA-smFISH signals (**Figure 2J,K**), further confirming the specificity of mtDNA-smFISH. Moreover, mtDNA-smFISH performed reliably in other developing and adult *Drosophila* tissues, including the wing imaginal discs, larval salivary gland, thoracic muscle and ovaries (**Figure S3J-M**). Together, these results demonstrate that mtDNA-smFISH can specifically label mtDNA molecules *in situ*, with single-molecule resolution, not only in human and *Drosophila* cell culture, but also in whole-mount tissues, thus opening the possibility for future studies of genetic mtDNA variation at subcellular or single-mitochondrion resolution.

175

176 **Immunofluorescence combined with mtDNA-smFISH**

177 Although we could successfully conduct anti-ATP-synthase (**Figure 1I-N**), anti-TOMM20 (**Figure**
178 **1K-P**), anti-TFAM (**Figure 1R-U**) and anti-Flag-tag (**Figure 2J-K**) IHC after the harsh denaturation
179 conditions of mtDNA-smFISH, this was not the case for most other epitopes, such as GFP (**Figure**
180 **S6**). Many epitopes do not tolerate denaturation as they change conformation upon fixation, heating
181 or formamide treatment. Although specific anti-heat denatured antibodies exist for GFP [63], allowing
182 anti-GFP immunostaining in whole-mount tissues after denaturation (**Figure 3A-D**), such reagents
183 are not available for most proteins or epitopes. We therefore developed a protocol that includes im-
184 munostaining with biotin-labelled antibodies prior to denaturation (**Figure 3E**), as biotin remains
185 intact during the denaturation step. When combined with a second round of fixation after primary
186 antibody incubation (see methods), this allows visualization of the primary antibody binding pattern
187 with a streptavidin-conjugated fluorophore post-mtDNA-smFISH (**Figure 3F,G**).

188

189 **mtDNA-smFISH to detect heteroplasmic mtDNA deletions**

190 Having established mtDNA-smFISH for sequence-specific *in situ* detection of single mtDNA mole-
191 cules, we next asked whether this approach would allow us to distinguish different mtDNA molecules
192 within the same cell. mtDNA deletions have previously been detected *in situ* in cultured human cells
193 by FISH using long probes [40]. We adapted mtDNA-smFISH for the same purpose, to detect mtDNA
194 heteroplasmy in human cybrid cells carrying a mixture of wild-type (WT) mtDNA and mtDNA mol-
195 ecules with a single large deletion (ΔH2.1) [64]. We designed one set of 12 probe pairs to specifically
196 label full-length, wild-type mtDNA molecules by targeting the mtDNA deletion sequence ('deletion
197 probes'), in addition to the human probe set we initially designed, recognizing all (i.e. deleted and
198 full-length) mtDNA molecules ('common probes') (**Figure 4A; Figure S1D,G,H; Table S1**). Spec-
199 ificity of all individual probe pairs was tested by conducting mtDNA-smFISH with each probe pair
200 at 100x concentration in cybrid cells before and after ddC-mediated mtDNA depletion (Rho^0 cells)
201 (**Figure S10**). This showed substantial differences in signal intensity between probe pairs (**Figure**
202 **S10A-C,G,H**). However, the intensity obtained in mtDNA-depleted Rho^0 cells was consistently
203 lower than in non-depleted cells (**Figure S10D-F,G,H**), apart from one probe pair (common probe 3;
204 **Figure S10G**), which was removed for further experiments.

205 We conducted mtDNA-smFISH using both human probe sets recognising either the deleted or non-
206 deleted sections of the human mtDNA for mtDNA-smFISH in ΔH2.1 cells with either low (**Figure**
207 **4B-E**) or high (**Figure 4F-I**) heteroplasmy. Single-cell heteroplasmy levels were quantified as the
208 percentage of mitochondrial localised (TOMM20-positive) puncta detected by the common probe set
209 that did not overlap with signal from the deletion probe set (**Figure S1H**), using a FiJi plugin for

automated heteroplasmy quantification in 2D (see methods). Because mtDNA-smFISH quantification was done in 2D, and detection of deleted molecules relies on a negative measurement (i.e. absence of signal from the 'deletion probes') (**Figure 4A**) without prior quantification of sensitivity for both probe sets, we cannot yet directly relate absolute single-cell heteroplasmy quantification in mtDNA-smFISH to ddPCR-based measurements. Nevertheless, mtDNA-smFISH could distinguish low from high heteroplasmy cell cultures (**Figure 4J;** 25.8%±9.5 (mean±sd) for low and 40.8%±10.6 (mean±sd) for high heteroplasmy), as confirmed by ddPCR-based quantification of single-cell heteroplasmy levels from the same cultures (**Figure 4K;** 3.8%±13.2 (mean±sd) for low and 66.2%±16.1 (mean±sd) for high heteroplasmy).

mtDNA-smFISH to detect mtDNA heteroplasmy *in vivo*

To study mtDNA heteroplasmy *in vivo*, we took advantage of a heteroplasmic *D. melanogaster* (Dmel) fly line that stably transmits a temperature-sensitive lethal mtDNA mutation in the CoI subunit of the cytochrome oxidase complex (*mt:CoI^{T300I}*) together with a functionally neutral 9bp deletion (*mt:ND2^{del1}*) in the ND2 subunit of Complex I [62]. The *mt:CoI^{T300I}* mutation impairs cytochrome oxidase activity at higher temperature (29°C), causing lethality at late pupal stages in homoplasmic flies [24,65]. Introducing WT mtDNA from *D. yakuba* (Dyak) species through germ-plasm transfer [66] rescues viability in *mt:CoI^{T300I}* flies [18,39,67]. As a result, these *D. melanogaster* flies (i.e. with a *D. melanogaster* nuclear genome) carry both the Dmel *mt:COI^{T300I}* mutant and Dyak WT mtDNA at high levels of heteroplasmy (**Figure 4L**).

We designed mtDNA-smFISH probes to distinguish Dmel (carrying the *mt:CoI^{T300I}* mutation) from Dyak (WT) mtDNA (**Figure S1C,E; Table S1**). The main sequence divergence between Dmel and Dyak mtDNA is in the non-coding D-loop, allowing FISH with long probes [39], but precluding single-molecule analysis. Due to its repetitive and AT-rich nature, this non-coding region is not amenable to smFISH with small probes. We therefore designed 7 (Dmel) and 5 (Dyak) probe-pairs across the most divergent coding regions characterised by small indels or multiple single-nucleotide polymorphisms (**Figure S1C**). mtDNA-smFISH in heteroplasmic larval brains yielded clear punctate cytoplasmic staining for both probe sets (**Figure 4M,N**), albeit weaker than mtDNA-smFISH with the common probe set consisting of 10 probe pairs (**Figure S3;S7**).

As with the other probe sets, no signal was detected in conditions without probes or amplifiers (**Figure S7A-L**). Testing specificity on brains from WT homoplasmic Dmel or Dyak flies (i.e. only containing WT *D. melanogaster* or WT *D. yakuba* mtDNA), showed that the Dmel probe set produced no signal in Dyak tissue (**Figure S7M-T**). Some punctate staining was observed with the Dyak probe set on homoplasmic Dmel tissues (**Figure S7O,S**), which was not due to a specific probe pair from the Dyak probe set (**Figure S8**). This background was considerably weaker than the signal obtained

in homoplasmic Dyak tissue (**Figure S7O,S,R,T**), allowing background correction if necessary during image analysis.

We quantified heteroplasmy levels manually in 3D in single NSCs using mtDNA-smFISH, and observed notable cell-to-cell variability in heteroplasmy levels, even between NSCs of the same brain (**Figure 4O-R**). On average, NSC heteroplasmy levels measured by mtDNA-smFISH were slightly lower than the levels obtained by pyrosequencing of whole adult flies of the same genotype (**Figure S9C-G; Figure 4S**), consistent with previously described age-dependent increase of mutant mtDNA heteroplasmy levels [19]. Large NSC-to-NSC heteroplasmy variability was also observed using pyrosequencing of mtDNA from FACS-sorted single NSCs with a different nuclear genomic background (Dpn::GFP; **Figure S9E**). Because mtDNA-smFISH allows direct *in situ* visualization of heteroplasmy, it now opens the possibility to investigate heteroplasmy shifts across different cells and tissues, eventually uncovering the underlying cellular and molecular processes controlling heteroplasmy regulation [11].

Purifying selection in the *Drosophila* female germline

Previous studies indicate that mtDNA molecules carrying deleterious mutations are subject to purifying selection during oogenesis in *Drosophila* [39,68-71]. These conclusions were mostly based on qPCR-analysis of mtDNA in homogenised ovaries and offspring from heteroplasmic female *Drosophila* [39,68-70], or on whole-tissue analysis with long FISH probes [39]. However, single-cell, single-molecule analysis of this process has not been possible, until recently [41]. We used our *in vivo* mtDNA-smFISH probes to label Dmel or Dyak mtDNA in the different compartments of heteroplasmic *Drosophila* ovaries, corresponding to different stages of germ-cell differentiation (**Figure 5A,B**). [72] Automated 3D quantification of mtDNA was conducted with FISH-Quant [73]. This showed a small but significant decrease in the percentage of mutant Dmel mtDNA between the regions of the germarium corresponding to stages 1+2a (53.1±3.9%, mean±sd) or 2b (52.0±6.0%, mean±sd) and stage 3 (48.5±2.7%, mean±sd) ($p=0.02$ and $p=0.03$ respectively) (**Figure 5C-E**). This decrease in mutant heteroplasmy levels was accompanied by a significant increase in absolute mtDNA copy number between stage 2b (477±166, mean±sd) and 3 (1113±468, mean±sd; $p=0.002$) (**Figure 5F**), in line with a previously proposed model whereby preferential replication of wild-type mtDNA allows purifying selection at this stage of germ cell development [41,68,70,74]. When imaging entire ovaries, we also noticed instances of large cell-to-cell variability in heteroplasmy levels in the nurse cell compartments (**Figure S11A-C**). This likely indicates that the mother-to-offspring bottleneck caused by low mtDNA levels in germline stem cells (GSCs) [31] and subsequent rapid replication during oogenesis and nurse cell formation, also enhances cell-to-cell variability in heteroplasmy levels for non-oocyte GSC-derived cell-types.

A somatic bottleneck during *Drosophila* neurogenesis

During development, many instances occur in which large stem cells undergo asymmetric division to self-renew and give rise to a much smaller differentiating daughter cell [75]. We asked whether this could also create a genetic bottleneck that increases variability in mtDNA heteroplasmy levels between daughter cells, similar to the pronounced heteroplasmy differences observed among offspring of the same mother [26]. A typical example occurs during *Drosophila* neurogenesis in the developing larval brain, where we found NSCs at third instar to be on average ~12x larger than their differentiating progeny (NSCs:115.9±21.9μm^3; progeny:9.5±4.2μm^3; mean±sd) (**Figure 6A-C**). We conducted mtDNA-smFISH with Dmel and Dyak probe sets on heteroplasmic brains expressing membrane-associated mCD8::GFP, specifically in NSCs and their direct progeny (*Worniu*-GAL4,UAS-mCD8::GFP) [76] and performed GFP co-immunostaining to identify individual NSC lineages (**Figure 6A,B**). Quantification of mtDNA puncta also showed an average ~12x reduction in total mtDNA molecules between NSCs and their progeny (NSCs:208.7±68.4; progeny:16.4±7.1; mean±sd) (**Figure 6D**), comparable to the observed cell size reduction (**Figure 6C**). The average mutant heteroplasmy level was 66.4±5.7% in NSCs and 48.6±11.8% in progeny cells (n=14 lineages from 3 brains; mean±sd) (**Figure 6E,F**).

Using a linear mixed-effects model on logit-transformed data with NSC lineage as a random effect, we found that progeny cells showed significantly greater heteroplasmy variability than NSCs **(Figure 6E-H)**. A likelihood ratio test (LRT) comparing a model allowing for different variances between cell types to a null model assuming equal variances, supported this increased variability (LRT = 11.39, $p = 0.0007$) (**Figure 6G**). We performed Monte Carlo simulation tests, to evaluate whether the increased heteroplasmy variance observed in progeny could be explained by a model of random mtDNA segregation. Null distributions for normalized heteroplasmy variance were generated by randomly partitioning mtDNA molecules from a parent NSC into progeny cells. The observed increase in heteroplasmy variance among progeny cells was not significantly different from the null distribution (two-tailed Monte Carlo $p = 0.1193$; **Figure 6H;S9D**). This supports the hypothesis that the ~12-fold reduction in mtDNA CN during asymmetric NSC division acts as a somatic bottleneck, increasing the variance in heteroplasmy levels in the progeny cells.

In addition to increased variance, the linear mixed-effects model revealed that progeny cells had significantly lower heteroplasmy than NSCs ($\beta = -0.751$, SE = 0.069, $p < 0.001$), with the odds of mutant relative to WT mtDNA in progeny cells 0.47 times of those in NSCs (**Figure 6C-G,I**). To test whether this could be explained by random segregation, we compared observed normalized heteroplasmy shifts to null distributions generated by Monte Carlo simulations. The observed shift was significantly different from the null distribution (two-tailed Monte Carlo $p = 0.0001$; **Figure 6I;S11E**), indicating

that the decrease in the proportion of mutant mtDNA from NSC to progeny cannot be explained by a stochastic bottleneck alone. To quantify the strength of the putative selective mechanism, we used Approximate Bayesian Computation (**Figure S11F,G**) and found strong evidence for purifying selection, with a selection model favoured over a pure drift model in all lineages (posterior probabilities of selection model between 0.713-1.0; 13/14 lineages with posterior probabilities >0.9) (**Figure 6J; S11H**). The median selection coefficient (s) was estimated to be s = -0.51 (range -0.32 to -0.64) (**Figure S11H**), indicating that mutant mtDNA was about half as likely as wild-type mtDNA to be present in progeny cells. Asymmetric NSC division and neuronal differentiation must, therefore, involve an as-yet-unknown mechanism of purifying selection that favours segregation or selection of functional mtDNA into neuronal progeny (**Figure 6J**).

Discussion

Heteroplasmy levels for a given mtDNA mutation can show striking cell-to-cell variability, even among the same cell type of a single organ. They also change dynamically over time and thereby may contribute to aging and pathogenesis of mitochondrial disorders [77]. Our understanding of the molecular mechanisms that drive or allow cell-type specific accumulation of mtDNA mutations remains limited [11], largely due to the inability to efficiently visualize mtDNA sequences in specific cells within their tissue context, and combine this with immunostaining and genetic manipulations. Here, we describe a robust method for visualizing mtDNA heteroplasmy in whole-mount *Drosophila* tissue and in human cells, using sequence-specific smFISH of mtDNA combined with HCR for enzyme-free signal amplification. mtDNA-smFISH enables efficient detection of mtDNA in various *Drosophila* tissues, including the brain, salivary gland, wing discs, muscles, and ovaries. We show that it provides high detection efficacy (>90%) comparing mtDNA-smFISH-based measurements of single-cell mtDNA content with single-cell ddPCR of mtDNA. Specificity was assessed in cell culture and whole-mount tissues by applying mtDNA-smFISH to comparable tissues or cells from other species (human, *D. melanogaster* or *D. yakuba*), in Rho^0 cells, upon RNAse treatment, and upon expression of a mitochondrial-targeted restriction enzyme to selectively degrade WT mtDNA.

Using this method, we visualized and quantified mtDNA CN and heteroplasmy levels *in vivo* in various developing *Drosophila* tissues, focusing on the female germline and the developing brain, two tissues with key importance for mitochondrial disease inheritance and presentation [78]. In heteroplasmic *Drosophila* developing brains, we noticed a cell-to-cell variability in heteroplasmy levels. This was evident among individual NSCs in the same brain, in line with single-NSC heteroplasmy measurements by pyrosequencing. However, cell-to-cell variability was significantly higher between postmitotic progeny, even when derived from a single NSC. NSCs undergo asymmetric divisions [75]

to produce ~12x smaller progeny, accompanied by a proportionate reduction in mtDNA CN from ~200 to ~16 mtDNA molecules per cell. This therefore gives rise to a subcellular somatic genetic bottleneck, whereby only a subset of NSC mtDNA molecules segregates into the differentiating progeny, enhancing genetic drift and inter-neuronal heteroplasmy variability (**Figure 6K**). Statistical modelling of this bottleneck supports our interpretation of mtDNA CN reduction as the main factor underlying increased heteroplasmy variance in NSC progeny. This is consistent with findings in mammals demonstrating an ongoing, linear increase in mtDNA variance over time [7,79]. Previous mechanistic studies in the germline bottleneck suggest that increase in variance is a stochastic process, caused by binomial partitioning of mtDNA molecules at cell division and random mtDNA turnover [80]. Many other instances of asymmetric cell division or cell size reductions occur throughout development and tissue regeneration, for example in hair follicles [32,33]. This is likely to lead to similar increases in heteroplasmy variance and may underlie the accumulation of clonal mtDNA mutations in some neurons, as observed in the brain [81].

The rapid segregation of mtDNA heteroplasmy which occurs due to a genetic bottleneck can also provide the substrate upon which purifying selection can act by exposing deleterious mtDNA mutations to subtle selection mechanisms [27,70,82-84]. In *Drosophila*, the developing brain in larvae was previously found to show stronger purifying selection against mutant mtDNA than other tissues like wing disc, gut, or the aging adult brain [19]. We found mutant mtDNA levels to be consistently lower in progeny than in the NSC they directly derived from, with our statistical analysis revealing signatures of purifying selection to reduce mean heteroplasmy levels in progeny cells. This suggests that neurogenesis is accompanied by an as-yet-unknown mechanism of purifying selection, to ensure that new-born neurons carry more functional mtDNA, limiting the potential deleterious impact of increased heteroplasmy variability caused by a somatic bottleneck. We also observed purifying selection at a well-characterised genetic mtDNA bottleneck during the early stages of *Drosophila* oogenesis. This modulates mother-to-offspring mtDNA inheritance, and has been studied extensively before, mostly through indirect measures like qPCR measurements of mtDNA heteroplasmy levels in offspring [18,39,69,70,74], and recently also with another approach for single-molecule visualization of mtDNA heteroplasmy [41]. Purifying selection in the female germline is thought to occur through a range of mechanisms, in particular autophagy/mitophagy of mitochondria with pathogenic mtDNA mutations [39,69], and preferential protein translation on the surface of mitochondria with WT mtDNA [70,74]. Selective mitophagy of mitochondria with damaged mtDNA has also been observed in *C. elegans* [85,86] and human cell culture [87]. However, within each NSC lineage, almost all progeny contained lower heteroplasmy than the NSC they derived from. Since we only quantified heteroplasmy in the most-recent born progeny, localized close to the parent NSC, it seems likely that, already upon NSC division, mtDNA is subject to asymmetric segregation of WT rather than mutant mtDNA. This is

reminiscent of previous observations in mammalian cells [88,89] and yeast [90-92], that stem cells can selectively segregate young/old mitochondria or WT/damaged mtDNA into daughter cells, and could be driven by the intricate molecular machinery that regulates asymmetric apico-basal apportioning of intrinsic NSC/progeny fate determinants in *Drosophila* neuroblasts [75,93]. It will be important to confirm these observations, determine which mechanisms act in NSCs and their progeny, whether these are conserved in other somatic tissues and between species, and whether and how recently-described mtDNA quality control mechanisms like nucleoidophagy [94-96] may act specifically on mitochondria containing WT or mutated mtDNA.

Together, the new insights gained from this work contribute to our understanding of mtDNA dynamics, and provide a valuable tool for investigating mitochondrial inheritance and evolution in various contexts, with potential to have broader implications for understanding human mitochondrial diseases, neurodegeneration and aging.

Limitations

mtDNA-smFISH cannot differentiate mitochondrial genomes that only differ by a single-nucleotide polymorphism, as several variants or small indels are needed to confer probe specificity. Precisely how much sequence divergence is required remains to be determined. Automated heteroplasmy quantification through freely accessible software (FiJi) was done in 2D, but more accurate 3D quantification was done either manually or relied on paid software (Matlab). Another limitation is that minor cross-reactivity was observed of *D. yakuba*-specific probes with *D. melanogaster* mtDNA, which can be addressed by adjusting thresholds for signal quantification. Nonetheless, when applied in the right heteroplasmic context, and combined with immunostaining and targeted genetic perturbations, mtDNA-smFISH constitutes a powerful novel approach for probing the cellular and molecular mechanisms that shape mtDNA heteroplasmy dynamics during development and aging.

Acknowledgements

We thank all lab members and F. Karam-Teixeira, T. Samuels and W. Staels for helpful discussions and advice; H. Choi and colleagues from Molecular Instruments for generously sharing reagents and advice; C. Moraes for sharing the H2.1 cybrid cell line; A. Harrison from the MRC MBU Imaging Facility for support with imaging; R. Schulte, G. Grondys-Kotarba from the CIMR Flow Cytometry Facility for assistance with cell sorting; A. Glynos, S. Burr, P. Nash for help with pyrosequencing and ddPCR; L. Bozhilova for advice on statistics and modelling. *Drosophila* stocks obtained from the Bloomington *Drosophila* Stock Center (NIH P40OD018537) were used in this study.

This work was supported by a Wellcome Clinical Research Career Development Fellowship (219615/Z/19/Z), an Evelyn Trust Medical Research Grant (21-25), and a UKRI BBSRC Responsive Mode Research Grant (BB/X00256X/1) to JvdA. PFC and JvdA are supported by a Wellcome Discovery Award (226653/Z/22/Z), a Medical Research Council (MRC) award (MC_PC_21046) to establish a National Mouse Genetics Network Cluster in Mitochondrial Diseases (MitoCluster), and the LifeArc Centre to Treat Mitochondrial Diseases (LAC-TreatMito) under grant no. 10748. LifeArc is a charity registered in England and Wales under no. 1015243 and in Scotland under no. SC037861. JP, PFC and JvdA acknowledge core funding from the UKRI MRC to the MRC Mitochondrial Biology Unit (MC_UU_00028/5, MC_UU_00028/7 and MC_UU_00028/8). HM was funded by a Wellcome Sir Henry Dale Fellowship (202269/A/16/Z) and an ERC Starting Grant (803852). BG acknowledges studentship funding from the Cambridge Trust and the China Scholarship Council.

For the purpose of open access, the authors have applied a Creative Commons Attribution (CC BY) licence to any Author Accepted Manuscript version arising from this submission.

Author contributions

RC, SG, AMHA and JvdA designed and conducted mtDNA-smFISH experiments. AD performed statistical analysis and modelling. BG and HM provided essential reagents and assisted with cell culture and ddPCR. SP assisted with *Drosophila* genetics and sample preparation. MF, SRC and LCT assisted with cell culture and image analysis. PFC, JP, HM and JvdA supervised the project and obtained funding. RC and JvdA wrote the paper, and all authors edited and approved the final manuscript.

Data availability

Image analysis and statistical modelling scripts are available on Github (https://github.com/JvdA-lab/mtDNA-smFISH). Further information and requests for resources and reagents should be directed to and will be fulfilled by the lead contact, Jelle van den Ameele (jv361@cam.ac.uk).

Declaration of interests

The authors declare no competing interests.

Materials and Methods

Key resources table

Reagent or Resource	Source	Identifier
***Drosophila* lines**		
UAS-mito-HA-GFP	BDSC	BDSC_8442
UAS-mito-HA-GFP,e1	BDSC	BDSC_8443
UAS-Mito-XhoI-Myc	BDSC	BDSC_81007
Mi(PT-GFSTF.0)dpnMI00051-GFSTF.0	BDSC	BDSC_59755
UAS-Mito-LbNox-Flag (in attP2)	This study	
Worniu-GAL4	BDSC	BDSC_2364
UAS-mCD8::GFP	BDSC	
w^{1118};;	BDSC	BDSC_5905
w^{1118};; (*D. yakuba* mtDNA)	Hansong Ma	
w^{1118};; (mt:$ND2^{del1}$+mt:CoI^{T300I}; *D. yakuba* mtDNA)	Hansong Ma	
Antibodies		
rat anti-Deadpan	Abcam	ab195173
chicken anti-GFP	Abcam	ab13970
mouse anti-ATPsynα	Abcam	ab14748
rabbit anti-FLAG M2	Cell Signalling	D6W5B
guinea pig anti-heat denatured GFP	Hiroyuki Hioki	
rabbit anti-heat denatured GFP	Hiroyuki Hioki	
rabbit anti-Tom20	Thermo Fisher Scientific	10G6I8
mouse Ig2a anti-T20	Santa Cruz	sc17764
Rabbit anti-TFAM	GeneTex	GTX103231
biotin-conjugated goat anti-Chicken IgY (H+L) secondary antibody	Invitrogen	PA1-28657
Alexa Fluor 488 Streptavidin	Abcam	ab272187
Chemicals		
Dulbecco's Modified Eagle Medium	Thermo Fisher Scientific	10566016

Fetal Bovine Serum	Thermo Fisher Scientific	16140071
Trypsin	Sigma-Aldrich	T2601
Prolong Diamond antifade mounting medium	Thermo Fisher Scientific	P36961
Formaldehyde	Thermo Fisher Scientific	28908
Formamide Deionized	Merck Millipore	S4117
TritonX-100	Sigma-Aldrich	STBJ7635
Tween20	Sigma-Aldrich	SLCH9711
20X SSC	Sigma-Aldrich	S6639
Hybridisation solution	Molecular Instruments	BPH02023
Washing buffer	Molecular Instruments	BPW002225
Amplification buffer	Molecular Instruments	BAM02622
DNeasy Blood and Tissue kit	Qiagen	69504
QIAamp DNA Micro Kit	Qiagen	56304
Power SYBR™ Green PCR Master Mix	Applied Biosystems	4367659
Phusion HF polymerase	NEB	NEB M0530
PyroMark PCR Kit reagents	Qiagen	PN:978703
PyroMark Q48 Autoprep	Qiagen	PN:974002
Magnetic Beads PyroMark Q48	Qiagen	PN: 1096484
Tris-HCl	Sigma-Aldrich	T8943
Proteinase K	NEB	P8107AA
ddPCR Supermix for Probes (no dUTP)	BIO-RAD	186-3010
Papain	Sigma-Aldrich	P4762
Collagenase	Sigma-Aldrich	C2674
Insulin	Sigma-Aldrich	10516
Penicillin and streptomycin (pen-strep)	Sigma-Aldrich	P4458
L-glutamine	Sigma-Aldrich	G7513
2',3'-Dideoxycytidine	Sigma-Aldrich	D5782
RNase A	Roche	10109142001

Drosophila strains and husbandry

Homoplasmic *Drosophila melanogaster* strains were maintained at 25ºC, and heteroplasmic strains carrying the temperature sensitive mt.COI^{T300I} mutation at 29ºC, unless indicated otherwise. The following stocks were used: UAS-mito-HA-GFP (BDSC_8442); UAS-mito-HA-GFP,e1 (BDSC_8443); UAS-Mito-XhoI-Myc (BDSC_81007); Mi(PT-GFSTF.0)dpnMI00051-GFSTF.0 (Dpn::GFP) (BDSC_59755); UAS-Mito-LbNox-Flag (A. Hynes-Allen and D. Dubal, unpublished). The GAL4-driver used throughout the study was Worniu-GAL4 on II [60] (BDSC_2364), either on its own or recombined with UAS-mCD8-GFP on II, to mark NSCs and their immediate progeny (where GFP expression perdures). Heteroplasmic *Drosophila*, carrying a combination of wild-type *D. yakuba* mtDNA and mutant *D. melanogaster* mtDNA (mt:ND2^{del1}+mt:CoI^{T00I}), on a nuclear *D. melanogaster* w^{1118} genomic background, were described previously [18]. Heteroplasmy was monitored routinely by PCR-restriction digest (see below; **Figure S7**). Apart from the experiments on ovaries, all experiments were done on both male and female larvae.

Cell culture

Drosophila melanogaster S2R+ cells were maintained in Schneider's *Drosophila* Medium (Thermo Fisher Scientific 21720024) supplemented with 10% fetal bovine serum (FBS) (Thermo Fisher Scientific 16140071), in a humidified incubator at 25ºC.

HeLa cells were cultured in Dulbecco's Modified Eagle Medium (DMEM) (Thermo Fisher Scientific 10566016) with 10% FBS (Thermo Fisher Scientific 16140071) in a closed 10ml dish at 37ºC, 5% CO2 and ambient O2. Medium was refreshed every other day. Upon reaching confluency (every 3-4 days), cells were detached using Trypsin (Sigma-Aldrich T2601) for 3-5 minutes, resuspended in culture medium, spun down at 200xg for 2 minutes at room temperature (RT), resuspended in 1 ml of fresh medium, and diluted 1:10 in a fresh culture dish.

H2.1 cybrid cells carrying a heteroplasmic mtDNA deletion (a patient-derived 7.5 kb partial deletion from m.7982 to m.15504) were obtained from Dr Carlos Moraes [64]. Cells were cultured in a 5% CO2 and 37ºC incubator in DMEM-high glucose-pyruvate (Gibco 41966), supplemented with 10% FBS (Gibco A5256701) and 50 µg/mL uridine (Sigma U3003).

Rho^0 cell line was derived from low heteroplasmy ΔH2.1 cybrid cells by adding 500µM of 2',3'-Dideoxycytidine (Sigma-Aldrich D5782) to media for 17 days.

Antibodies

The following primary antibodies were used: rat anti-Deadpan (1/100, Abcam ab195173); chicken anti-GFP (1/500, Abcam ab13970); mouse anti-ATPsynα (1/500, Abcam ab14748); rabbit anti-FLAG

M2 (1/500, Cell Signalling D6W5B); Guinea pig or rabbit anti-heat denatured GFP (1/500, kind gift of Hiroyuki Hioki [97]); rabbit anti-Tom20 (1/500, Thermo Fisher Scientific 10G6I8); Rabbit anti-TFAM (1/200, GeneTex GTX103231); mouse Ig2a anti-Tom20 (1/200, Santa Cruz sc17764). Secondary antibodies for conventional immunostaining were Alexa Fluor 405, 488, 546, 647 -conjugated secondary antibodies raised in goat or Donkey (1/500, Life Technologies). For biotin-labelled immunostaining, we used biotin-conjugated goat anti-Chicken IgY (H+L) secondary antibody (1/500, Invitrogen PA1-28657) and Alexa Fluor 488 Streptavidin (1/250, Abcam ab272187).

mtDNA-smFISH probes.

mtDNA-smFISH probes for third-generation FISH-HCR [47,49] were either ordered from Molecular Instruments (lot numbers PRH253 and PRJ122 for Dyak-specific probes; PRH254 and PRJ123 for Dmel-specific probes; PRH417 for *Drosophila* common probes), or designed in-house (for all human probes) and ordered as desalted unmodified oligonucleotides (Sigma). The probe design process from Molecular Instruments is proprietary, but probes were designed to maximize sequence divergence by including at least a small indel, contained within one of the probe halves. Probes were designed against a target sequence of 52 base pairs, with two halves designed against 25 base pairs on either side, separated by two base pairs. Initiator and spacer sequences for each set of amplifiers were as in [47,50]. Oligonucleotides were then assembled as follows: (probe half 1) Initiator1 - I1spacer - Reverse complement of 5'side of target sequence ; (probe half 2) reverse complement of 3'side of target sequence - I2spacer - Initiator 2. Target sequences, and probe sequences for in-house designed probes are shown in **Table S1**. Probe pair number 3 was removed from the human common and deletion probe sets (Figure S10).

Whole-mount mtDNA-smFISH.

Larval tissues were dissected in PBS, fixed in 4% formaldehyde (FA) in phosphate buffer saline (PBS) with 0.3% TritonX-100 (Sigma-Aldrich STBJ7635) (0.3%PBSTx) for 30 minutes at RT, and washed for 3 × 5 minutes in 0.1% PBSTx at RT. Fixed tissue underwent dehydration through consecutive washes in cold PBS with 0.1% Tween20 (Sigma-Aldrich SLCH9711) (PBSTw) with 25%, 50%, 75%, and 100% methanol for 10 minutes each at 4°C. Tissue can be stored at -20°C at this stage, until *in situ* hybridisation (ISH). Prior to ISH, tissues were rehydrated through consecutive washes in cold PBSTw with 100%, 75%, 50% and 25% methanol for 10 minutes each, and a final wash in PBSTw. Denaturation solution was 70% Formamide (Merck Millipore S4117), 2x saline-sodium citrate (SSC) (Sigma-Aldrich S6639) in H_2O. Tissues were incubated in 600µl denaturation solution at 90°C in a shaking heating block at 300rpm for 10 minutes. Probes were stored at 1µM stock solution (i.e. 1µM for each probe half) at -20°C, defrosted prior to ISH, and 0.8µl was added to 200µl hybridisation

solution (Molecular Instruments BPH02023; stored at -20 ºC), for a final hybridisation concentration of 4nM for each probe-half. Final total hybridisation concentration therefore depends on the number of probes in each probe set. For smaller probe sets (i.e. Dmel and Dyak specific probe sets targeting 7 and 5 sequences respectively), concentration was increased to up to 40nM, to improve signal intensity. Probes were heated in hybridisation solution to 95ºC for 2 minutes. Denaturation solution was removed from the tissues and replaced by the heated hybridisation solution with probes. Heating block temperature was adjusted to 37ºC, to rapidly but gradually cool the tissues with probes, and then incubated overnight at 37ºC in a shaking heat block. In the meantime, washing buffer (Molecular Instruments BPW002225; stored at -20ºC) was placed in a 37ºC incubator to pre-warm. The following day (day 2), tissues were washed 4 x 15 minutes with warmed probe wash buffer at 37ºC (for the first wash, wash buffer was added to the sample directly to make tissues sink to the bottom of the vial), followed by a 5 minutes wash in 50% probe wash buffer and 50% 5xSSC with 0.1% Tween20 (SSCT) at RT and two final 5 minutes washes with SSCT at RT. HCR amplifiers were defrosted in the dark, and annealed by placing 2µL (of 3µM stock for 6pmol final concentration per sample) of each hairpin in separate tubes, heated to 95ºC for 1.5 minutes and cooled at RT in the dark. Next, all HCR hairpins were combined and added to amplification buffer (Molecular Instruments BAM02622; stored at 4 ºC; 100µL per sample), if necessary, with nuclear counterstain DAPI (4',6-diamidino-2-phenylindole) at 1:500, added to the tissue sample and incubated in the dark overnight at RT. The final day (day 3) consists of washes with SSCT of 2 x 5 minutes, 2 x 30 minutes, and 1 x 5 minutes, followed by 3 x 10 minutes washes with 0.1%PBSTx and 2 x 10 minutes with PBS. Tissues were mounted in ProLong Diamond antifade mounting medium (Thermo Fisher Scientific P36961). Slides were stored at 4°C and imaged after 24 hours.

mtDNA-smFISH on cultured cells

HeLa, H2.1 cybrids or S2R+ cells were cultured in IBIDI 12-Well Chambers (Thistle Scientific IB-81201) in 250µL of medium, the maximum capacity for the wells. Cells were fixed using 4% FA in PBS containing 0.1% PBSTx, washed in PBSTx, and subjected to dehydration and rehydration steps as per the smFISH protocol. Only for individual probe testing (**Figure S10**), hybridisation was performed with a final hybridization concentration of 400nM for each probe-half. For heating during the pre-hybridisation step, the IBIDI plate was placed on a flat surface of an inverted heating block underneath a polystyrene cover. For probe hybridisation, the IBIDI wells were placed in a wet chamber to prevent evaporation. This chamber was created by placing pre-warmed, wet tissue paper at the bottom of an empty pipette tips box, with the IBIDI wells on top. The box was maintained at 37°C in an incubator. Subsequent wash steps, and antibody staining were essentially as for the whole-mount smFISH-HCR protocol, as described above. RNase treatment was performed on H2.1 cybrid cells

after fixing and permeabilizing with PBSTx. The treatment was conducted as described previously [98] with 1 hour incubation at 37ºC in 100µg/mL RNase A (Roche 10109142001). Samples were washed three times in PBS and protocol was continued as previously described, resuming from the dehydration and rehydration steps.

Incorporating immunostaining with mtDNA-smFISH.

For conventional antibody staining of epitopes not affected by heat denaturation (anti-Flag, anti-TOMM20, anti-ATPsyna, anti-TFAM immunostaining), or with antibodies against heat denatured GFP [97], immunostaining was conducted after the smFISH protocol. In the final washes, 5xSSCT was replaced by 0.3%PBSTx through serial washing with 75%, 50% and 25% 5xSSCT in PBSTx for 5 minutes each, and 3 x 5 minutes in PBSTx. For immunostaining, brains were incubated with primary antibodies in 0.1%PBSTx overnight at 4ºC, washed with 0.1%PBSTx, incubated with secondary antibodies in PBSTx overnight at 4ºC and washed with 0.1%PBSTx. Brains were mounted in Prolong Diamond antifade mounting medium (Thermo Fisher Scientific P36961).

For biotinylated antibody staining, primary and secondary biotinylated antibody staining followed by a second fixation step were conducted before the smFISH protocol. After the rehydration step on day 1, tissues were incubated with anti-GFP chicken primary antibody (Abcam ab13970; 1:500) in 0.1% PBSTx overnight at 4ºC. The following day (day 2), tissues were washed 3 x 10 minutes with 0.1% PBSTx, and incubated overnight with goat biotinylated anti-chicken IgY (H+L) secondary antibody (Invitrogen, PA1-28657; 1:500). The next day (day 3), tissues were washed 2 x 5 minutes with 0.1% PBSTx, followed by a second fixation in 4% FA in 0.1% PBSTx for 20 minutes at RT, and washed 2 x 5 minutes in PBSTw, to next continue with the mtDNA-smFISH denaturation steps and protocol. In the final washes of the smFISH protocol, the tissues were processed as described above for conventional immunostaining, but after the final wash in 0.1%PBSTx, incubated overnight with streptavidin Alexa Fluor 488 conjugate at 1:100 (Jackson Immunoresearch 016-540-084). The final day, 3 x 10 minutes washes were done with 0.1%PBSTx, and 2 x 10 in PBS prior to mounting in Prolong Diamond antifade mounting medium (Thermo Fisher Scientific P36961).

***Drosophila* larval brain dissociation and fluorescence-activated cell sorting**

Dissociation of *Drosophila* larval brain tissue was done essentially as described previously [99]. About 50 L2/L3 larval brains were dissected in ice-cold PBS and transferred to an Eppendorf low binding microcentrifuge tube with 100µl of ice-cold Rinaldini's solution (800mg NaCl, 20mg KCl, 5mg NaH_2PO_4, 100mg $NaHCO_3$, 100mg glucose in 100ml distilled H_2O; filtered through Millipore Steriflip (pluriSelect); 10x can be stored at 4ºC). Brains were centrifuged at 300g for 3 minutes at 4ºC and the supernatant replaced with dissociation solution (445µl Schneider's medium, 50µl papain (Sigma-

Aldrich P4762) and 5µl collagenase (1mg/ml, Sigma-Aldrich C2674) (Schneider's culture medium consists of 2.5ml FBS (Thermo Fisher Scientific 16140071), 50µl insulin (Sigma-Aldrich 10516), 500µl pen-strep (Sigma-Aldrich P4458), 2.5ml L-glutamine (Sigma-Aldrich G7513) in 18.925ml Schneider's medium (Thermo Fisher Scientific 21720024) and filtered through Millipore Steriflip (pluriSelect). Tissues were incubated at 30ºC in a shaking heat block for one hour, with gentle pipetting every 15 minutes. Next, dissociated cells were centrifuged at 300xg for 3 minutes at 4ºC, washed with 1ml ice-cold Rinaldini's solution and centrifuged at 300xg for 3 minutes at 4ºC. Subsequently, 200µl Schneider's culture medium was added, cells resuspended by 10-20 times pipetting with a 200µl pipette tip, centrifuged again at 300xg for 3 minutes at 4ºC and finally resuspended in 400µl PBS with 0.04% bovine serum albmin (BSA). The cell suspension was filtered through a 10µm pluriStrainer (Cambridge Bioscience 43-50010-03), after wetting the filter with 200µl PBS with 0.04%BSA.
Fluorescence-activated cell sorting (FACS) was carried out on a Melody^{Tm} Cell sorter (BD Biosciences), and data analysis was conducted on FlowJo software (BD Biosciences). The cell suspension after tissue dissociation was transferred to a 5ml 12x75mm style (Falcon) polystyrene round bottom tube with a cell strainer cap, and kept on ice before FACS. FACS settings were optimised to keep living and non-permeabilised cells (DAPI-negative and DRAGQ5) (**Figure S3**) and single or specific numbers of Dpn::GFP-positive cells were collected in a 96-well PCR plate. Plates were immediately stored at -80ºC for future downstream processing.

Droplet Digital PCR (ddPCR)

ddPCR was conducted as described previously [100]. For mtDNA CN measurements with ddPCR on sorted NSCs, cells were processed in a 96-well plate, either as single cells, or as sets of 10, 20, 50 or 100 cells. In ΔH2.1 cells, analysis was performed as single cells only. Cells were lysed in 2.5µL lysis buffer consisting of 50mM Tris-HCl (Sigma-Aldrich Trizma T8943) at pH 8.3, TWEEN-20 (Sigma-Aldrich SLCH9711), and 200µg/mL Proteinase K (New England Biolabs P8107AA). Plates were centrifuged at 1,000 x g for one minute at 4°C, incubated at 37°C for 30 minutes in a thermocycler with the lid heated at 105°C, and Proteinase K was next heat inactivated for 15 minutes at 80°C. 7.5µL of nuclease-free water was added to each sample to a final volume of 10µL, and plates were centrifuged at 1,000 x g for one minute at 4°C. The cell lysate was stored at -20°C before proceeding with ddPCR if needed. ddPCR Master mix for 1 reaction consists of 12.5µL 2x ddPCR Supermix for probes (BIO-RAD 186-3010), 1.25µL of 20x VIC or HEK (depending on the experiment), 1.25µL of 20x FAM probes and 7µL of sterile water, to a final volume of 22µL, and vortexed after preparation. In cybrid cell lines a FAM and a HEX probe were used for MT-ND4 and MT-ND1 respectively, as previously described [100]. PCR primer sequences (all 5'-3') were: huND4 Forward primer AGTGCGATGAGTAGGGGAAGG; huND4 Reverse primer ACCTTGGCTATCATCACCCGAT;

huND1 Forward primer GGGTTCATAGTAGAAGAGCGATGG; huND1 Reverse primer ACGCCATAAAACTCTTCACCAAAG. Probe sequences were (all 5'-3'): huND4 (FAM) CAACCAGCCAGAACGCCTGAACGCA; huND1 (HEX) ACCCGCCACATCTACCATCACCCTC.
For *Drosophila* mtDNA CN determination with ddPCR, VIC targets both Dmel and Dyak mtDNA, while FAM targets only Dmel mtDNA (**Figure S5A**). PCR primer sequences were (all 5'-3'): Dyak+Dmel PCR Forward, AACAGACTTAAAATTTGAACGGCTACAC; Dyak+Dmel PCR Reverse, GGAGAGTTCATATCGATAAAAAAGATTGCG; Dmel PCR Forward, CTTCCAGTACTAGCAGGAGCTATT; Dmel PCR Reverse, CCTCCTCCCGCTGGGT. Probe sequences were (all 5'-3'): *D. yakuba* and *D. melanogaster* mtDNA (VIC), TATATCTTAATCCAACATCGAG; *D. melanogaster* mtDNA (FAM), ATCGAAATTTAAATACATCATTTTTT. 22µL master mix was added to each well of a new 96-well plate, and 3µL of DNA from the lysed cells, or nuclease-free water to the non-template control wells to bring total volume to 25µL. Plates were sealed, centrifuged at 1,000 x g for 1 minute at 4°C and transferred to the droplet generator. Once droplets were formed, PCR was performed for 40 cycles with denaturation at 94°C for 30 seconds and annealing and extension at 58°C for 1 minute. Finally, the 96-well plate is placed in the droplet reader for analysis. mtDNA CN was calculated as follows: mtDNA target concentration/µL x 25 x 1/fraction of total lysate input. FAM probe was specific for Dmel mtDNA (**Figure S5B**), and mtDNA CN calculations of Dmel mtDNA across a range of mtDNA concentrations were similar for FAM and VIC probes (**Figure S5C,D**). mtDNA CN scaled according to cell numbers (**Figure S5C-H**), further validating the assay and allowing to plot all per-cell values from these assays together. The assay variability was higher among single cells than among sets containing a group of cells (10, 20, 50 or 100), possibly due to cell doublets caused by inefficient FACS sorting, and single-cell ddPCR results were not included in final analysis (**Figure 2D;S5F,H**).

PCR restriction digest to determine *Drosophila* heteroplasmy.

We developed a straightforward genotyping approach, to monitor Dmel and Dyak heteroplasmy levels, taking advantage of an NdeI restriction site in the Dyak mtDNA (**Figure S9A**), with NdeI retaining 100% in most PCR buffers. Genomic DNA was extracted from whole flies or dissected with QIAamp DNA Micro Kit (QIAGEN 56304). PCR was done with Phusion HF polymerase (New England Biolabs, ID: NEB M0530), for 30 cycles at melting temperature of 45°C, using the following primers common to both Dmel and Dyak mtDNA: Forward 5'-TTAGACCAAATTTATTGGGAGACCC-3' and Reverse 5'-GGAATTCCTCAACCTTTTTGTGATGC-3', resulting in 1283bp Dmel and 1288bp Dyak fragments. NdeI (NEB R3131) digests the Dyak but not Dmel mtDNA, resulting in 2 smaller fragments (425 and 859bp) (**Figure S9B**). Heteroplasmy levels were inferred by measuring intensity

of the smaller Dyak bands vs the larger Dmel band (**Figure S9B**), either after imaging of the agarose gel, or on a Tapestation (Agilent).

Bulk and single-cell pyrosequencing of *Drosophila* mtDNA variants

In order to accurately measure heteroplasmy levels with high sensitivity in single cells, we developed a pyrosequencing approach [101,102] to distinguish Dyak from Dmel mtDNA (**Figure S9C-F**). Pyrosequencing was done using the QIAGEN protocol, with PyroMark PCR Kit reagents (QIAGEN PN:978703), and primer design according to the PyroMark Assay Design SW 2.0 quick start guide. We determined optimal annealing temperatures for several primer pairs to allow efficient PCR amplification of the mtDNA target region. Validation was conducted through pyrosequencing of homoplasmic Dyak or Dmel animals on a standard curve of mixed PCR products (**Figure S9E,F**) and by comparing two different sets of primers (ID8 and ID9), together confirming the accuracy of heteroplasmy detection. Pyrosequencing primers (all 5'-3') were Forward-8 TTTAATATTTGGTCCTTTCGTACT and Reverse-8 AGCCAGGTTGGTTTCTATCTTTAA, with sequencing primer GGTTTCTATCTTTAAAAAAT; Forward-9 GCTACCTTTGCACAGTCAAAATAC and Reverse-9 GTTTAAATAAAGAATTCGGCAAAA, with sequencing primer TTTGTTAAACAGGCGA. Pyrosequencing of heteroplasmic animals yielded reproducible results (**Figure S9E,F**), with values in line with our first PCR- and digestion-based method (data not shown), and with an independent, previously validated qPCR-based method [67] (**Figure S9E,F**).

Single-cell pyrosequencing was conducted on sorted NSCs (**Figure S4**). Before processing, the 96-well plate was spun down at maximum speed (2204xg) at 4℃ for 20 minutes, and samples were processed in a dedicated PCR hood with UV treated equipment. PyroMark PCR Master mix was pipetted straight onto the single-cell 96-well PCR plate, spun down for 1 minute at 300xg and PCR was for 45 cycles with melting temperature of 62ºC. 2µl of the PCR was verified on a 0.9% agarose gel, and PyroMark Q48 Autoprep (Qiagen) was used to conduct pyrosequencing of 10µl sample in a 48-well disc pyrosequencing plate with 3µl of Magnetic Beads PyroMark Q48 (PN:1096484).

Quantitative PCR (qPCR) of ΔH2.1 single mtDNA deletion heteroplasmy

DNA was isolated from ΔH2.1 cell lines using DNeasy Blood and Tissue kit (Qiagen #69504) according to the protocol. qPCR was performed to assess mitochondrial DNA (mtDNA) levels relative to nuclear DNA using β-actin as nuclear reference gene and ND1, COX3 and D-loop as mtDNA markers. PCR primer sequences were (all 5'-3'): β-actin Forward CACCATTGGCAATGAGCGGTTC; β-actin Reverse AGGTCTTTGCGGATGTCCACGT; ND1 Forward GGCTATATACAACTACGCAAAGGC; ND1 Reverse GGTAGATGTGGCGGGTTTTAGG; COX3 Forward AATCCAAGCCTACGTTTTCACACT; COX3 Reverse TAGGCCGGAGGTCATTAGG;

D-loop Forward CACCCAAGAACAGGGTTTGT; D-loop Reverse TGGCCATGGGTATGTT-GTTAA. Essay was performed using Power SYBR™ Green PCR Master Mix (Applied Biosystems #4367659) on a QuantStudio3 qPCR system. Each reaction contained 10 µL of SYBR Green Master Mix, 0.5 µM of each primer, and 30ng of total DNA template. PCR thermal cycling protocol consisted of: initial denaturation at 95 ºC for 10 min, followed by 40 cycles of 95 ºC for 15 s and 60 ºC for 1 min. A melt curve analysis was performed at the end to confirm amplification specificity. Relative mtDNA levels were calculated using the ΔCt and normalizing to the nuclear marker. Fold change was determined as 2^(-ΔΔCt). All reactions were performed in technical triplicates for all three experiments.

Confocal and Airyscan laser scanning microscopy

Fluorescent images were acquired using a Zeiss LSM880 confocal microscope, equipped with Fast AiryScan, with a 63x oil immersion objective, as 12- or 16-bit images. ΔH2.1 and Rho^0 cells were imaged using a 100× objective lens (NA1.4) on a Nikon Eclipse TiE inverted microscope with a 4-channel integrated laser engine (ILE-400) using an Andor Dragonfly 500 spinning disk system, equipped with a Zyla 4.2 PLUS sCMOS camera, coupled with Fusion software (Andor). All images are single sections, unless indicated otherwise. For whole-mount quantifications, slice thickness was ~0.8µm, with a 1/3 step size, ensuring complete NSCs or germaria were imaged and reconstructed. For ΔH2.1 cell quantification, seven sections of 0.2 µm each were acquired. All images from a same experiment were acquired with the same parameters including exposure time and laser intensities. Images were processed for brightness and contrast using ImageJ. Images shown in the figures were smoothed once in FIJI, and intensity and contrast were set to same levels within the same experiment.

Image analysis

Cell culture mtDNA-smFISH image pre-processing: Four-channel fluorescence microscopy images were acquired containing signals for common probe-set (CP, Channel 1), deletion probe-set (DP, Channel 2), mitochondrial outer membrane marker TOMM20 (T20, Channel 3), and TFAM (TF, Channel 4). Image processing and quantitative analysis were performed using custom ImageJ macros. Analyses of cell-culture images were performed on maximum-intensity projections of each z-stack to consolidate near-diffraction-limited nucleoid puncta across planes, boost signal-to-noise, and avoid slice-to-slice redundancy or z-registration artefacts when quantifying spots and colocalization. Following acquisition, regions of interest (ROIs) were manually selected using polygonal selection tools to isolate individual cells or mitochondrial networks. The selected regions were cropped after clearing pixels outside the ROI boundary, ensuring analysis was restricted to biologically relevant areas while maintaining the original four-channel structure. The CP and DP channels underwent identical

preprocessing to enhance nucleoid visualization. Background fluorescence was removed using a rolling ball algorithm (radius = 50 pixels), followed by initial Gaussian blur ($\sigma = 2$) to reduce noise. To sharpen nucleoid signals and improve spot detection accuracy, a custom deconvolution step was implemented using a 5×5 Laplacian kernel with centre weight of 24 and surrounding weights of -1, applied through convolution filtering with normalization. This deconvolution approach enhanced the point spread function of individual nucleoids while suppressing diffuse background fluorescence, critical for accurate quantification of discrete mtDNA foci. The deconvolved signals underwent morphological minimum filtering (radius = 2 pixels) to remove spurious peaks, followed by a final Gaussian blur ($\sigma = 2$) to smooth the enhanced features while preserving nucleoid centres. The anti-TOMM20 mitochondrial marker channel was processed with background subtraction (rolling ball radius = 50 pixels), contrast enhancement (0.35% saturation), and Gaussian blur ($\sigma = 2$) applied iteratively to generate a clean mitochondrial network signal. Binary masks were created using Otsu's automatic thresholding to define mitochondrial boundaries. TF channel immunofluorescence signals underwent background subtraction with a smaller rolling ball radius (20 pixels) to preserve finer structural details, followed by iterative contrast enhancement and Gaussian blur ($\sigma = 2$). An additional round of background subtraction was applied to eliminate residual cytoplasmic signal before final contrast adjustment.

Cell culture mtDNA-smFISH CP/DP Colocalization Analysis within Mitochondria: Processed CP and DP channels were masked with the anti-TOMM20 mitochondrial network staining to restrict analysis to mitochondrial regions. To preserve intensity information critical for accurate spot detection, two parallel versions of each masked image were maintained: intensity-preserved 32-bit images for quantitative analysis and user-adjustable thresholded versions for visualization. Spot detection utilized the Find Maxima algorithm with prominence thresholds of 15 for CP and 12 for DP, optimized for each channel's signal characteristics. Colocalized spots were identified through coordinate-based proximity analysis, where DP spots within three pixels of any CP spot were classified as colocalized. This distance-based approach ensured robust colocalization detection without requiring pixel-perfect overlap. Normalization calculations were performed to determine the ratio of colocalized DP spots to individual channel counts. Deletion percentages representing CP nucleoids without associated DP signal were calculated as [(CP spots - colocalized dP spots)/CP spots] × 100.

Cell culture mtDNA-smFISH CP-TFAM Colocalization Analysis: This pipeline quantified CP nucleoid association with TFAM signal. Following TOMM20 mitochondrial network masking of CP signals, an additional TF mask was applied using Otsu's automatic thresholding to identify CP spots within TFAM-positive regions. Intensity-preserved 32-bit images were maintained throughout all

masking operations to ensure accurate spot detection via the Find Maxima algorithm (prominence = 15). Sequential mask application first restricted CP analysis to the T20-defined mitochondrial network, then further refined detection to TFAM-positive subregions within mitochondria. The percentage of CP nucleoids colocalized with TFAM was calculated as [(CP spots in T20∩TFAM)/(CP spots in T20)] × 100, revealing the proportion of mitochondrial CP nucleoids residing in TFAM-enriched domains.

Whole-mount tissue mtDNA-smFISH analysis: NSC progeny (i.e. NSC together with their latest-born progeny) were identified through perdurance of mCD8::GFP expression after activation in NSCs using Worniu-GAL4, with cells closest to the NSC considered most-recently born [103]. For automated quantification of heteroplasmy in NSCs in 3D, stacks were cropped to individual NSCs, and MorphoLibJ [104] was used for segmentation of the Worniu-GAL4,mCD8::GFP IHC signal, to create a mask for downstream quantification with FishQuant [105]. Segmentation of germaria was performed manually in the X-Y axis, maintaining the entire imaging Z-stack for 3D quantification. mtDNA-smFISH puncta were quantified using FishQuant [105], following the standard protocol outlined in the online user manual, using either the germarium or the NSC mask as input. For cell or germarium segmentation, the "Define Outline" tool was used to manually trace individual cells using the polygon selection tool; background filtering was applied using the 3D_2XGauss method with a kernel size of 5 pixels in both the XY and Z dimensions (Kernel BGD XY,Z: 5,5), and a kernel signal-to-noise ratio (SNR) of 0.5 in both XY and Z (Kernel SNR XY,Z: 0.5,0.5). Spot detection thresholds were then manually optimised to ensure accurate puncta selection, with lower thresholds capturing more background signals. Once an appropriate threshold was established, the selection and parameters were saved for consistent application across samples, including both *Drosophila melanogaster* and *Drosophila yakuba*, to maintain comparability between datasets, and applied as batch mode for other replicates. When NSCs were difficult to segment, we instead used the CellCounter plugin in FiJi [106] to count mtDNA puncta manually. For Worniu-GAL4 x UAS-mitoGFP or UAS-mitoXhoI experiments, NSCs were delineated based on GFP-expression or nuclear morphology (DAPI) and mtDNA spots quantified manually; NSCs not expressing Worniu-GAL4[103] were determined based on typical location within the VNC. Occasionally, gaussian blur was applied to NSC images prior to segmentation or quantification.

Signal and background quantification: similar areas of the larval ventral nerve cord were selected in ImageJ/FiJi [106,107], or entire ΔH2.1 and Rho^0 cell images were saved as .tiff files, and imported in Matlab (The MathWorks Inc.), where the number of pixels at a given intensity value in 256 bins was quantified. Intensity distribution graphs are shown at a log scale to enhance differences in the lower values.

Data Output and Visualization: All pipelines generated binary masks, spot detection overlays, and quantitative results including total spot counts, colocalization percentages, and normalized ratios. Processed images and numerical results were automatically saved, with spot detection visualizations provided for quality control and validation of the automated counting algorithms. Graphs were made using R Statistical Software (v4.1.2; R Core Team 2021), [108] and figures were compiled in Affinity Designer.

Statistical analysis and modelling

For each experiment, the number of brains analysed ranged from 1-10. Each experiment where statistical analysis was performed included at least three biological replicates in cell culture experiments, and at least two in *Drosophila* experiments. Prism (GraphPad Software) and Excel (Microsoft) were used to perform statistical tests for Figure 2H; 5D,E; S2G: Shapiro-Wilk and F-tests to verify normality and variance, and t-tests, Wilcoxon signed rank, or Mann Whitney U test with Holm-Bonferroni multiple comparisons correction to determine significance.

Differences in heteroplasmy variance between NSCs and progeny were statistically tested using a linear mixed-effects model to account for non-independent measurements from the same cell lineage. Heteroplasmy percentages were first converted to proportions (h) and then logit transformed using the formula $logit(h) = \ln(h/(1-h))$ after squeezing values of 0 and 1 to satisfy the assumptions of normality and constant variance. The models included cell type (NSC or progeny) as fixed effect and cell lineage as random effect. A likelihood ratio test (LRT) was performed to compare a null model assuming equal variances (Model 0) to an alternative model allowing for different variances for each cell type (Model 1), implemented with the `varIdent` structure in the `nlme` R package. [109]

Model 0 (equal variances for NSC and progeny): $logit(h_{ij}) = \beta_0 + \beta_1 \cdot (cell\ type)_{jk} + u_i + \varepsilon_{ij}$, where $u_i \sim N(0, \sigma_u^2)$ and $\varepsilon_{ij} \sim N(0, \sigma^2)$

Model 1 (unequal variances for NSC and progeny): $logit(h_{ij}) = \beta_0 + \beta_1 \cdot (cell\ type)_{jk} + u_i + \varepsilon_{ij}$, where $u_i \sim N(0, \sigma_u^2)$ and $\varepsilon_{ij} \sim N(0, \sigma_k^2)$

Here, i indexes cell lineage, j indexes individual observations, k indexes cell type of observation j. u_i represents the random intercept for lineage i and ε_{ij} represents the residual error with variance σ_k^2 specific to cell type k in Model 1. For the LRT, both models were fitted using Maximum Likelihood (ML). Parameter estimates (β-coefficients and standard errors) were extracted from the best-fitting model, which was subsequently refitted using Restricted Maximum Likelihood (REML) for unbiased estimation. Statistical significance was assessed at the $\alpha = 0.05$ level. We used Monte Carlo simulations to test whether observed heteroplasmy dynamics were consistent with a null model of random

mtDNA segregation. For each of the NSC lineages, we simulated partitioning of mtDNA from the parent NSC into its set of progeny cells 10,000 times, using hypergeometric sampling, which models sampling without replacement and thus accounts for the progressive reduction of the parental mtDNA pool. The size of each draw was set to the experimentally observed mtDNA copy number of the corresponding progeny cell. The normalized heteroplasmy variance and shift were calculated for both observed and simulated data. We calculated normalized heteroplasmy variance for a cell-population with heteroplasmies $h = (h_1, h_2, \ldots, h_n)$ where n is the number of cells in the population and mean heteroplasmy $\bar{h}$ as $V'(h) = Var(h)/(\bar{h}(1-\bar{h}))$. [110] The normalized heteroplasmy shift from an NSC to a progeny ($\Delta h'$) was calculated as $\Delta = ln\left(\frac{h_{Progeny}(1-h_{NSC})}{(1-h_{Progeny})h_{NSC}}\right)$. [111] To generate test statistics comparable to the observed data, we calculated the mean normalized heteroplasmy variance and shifts across all NSC lineages for each simulation iteration. This produced null distributions of 10,000 values for each test statistic under the assumption of random segregation. Statistical significance was assessed by calculating two-tailed p-values as $p = (k+1)/(n+1)$, where k is the number of simulated statistic values that deviated from the null distribution mean by atleast as much as the observed statistic value, and $n = 10{,}000$ is the total number of simulations. The standard errors on the null distribution means were 1.32×10^{-4} for normalized heteroplasmy variance and 9.02×10^{-4} for normalized heteroplasmy shift, confirming adequate precision for reliable inference.

We used Approximate Bayesian Computation (ABC) to perform formal model comparison between a pure drift and a selection model and to quantify the strength of selection required to explain the reduction in heteroplasmy levels observed in progeny cells. Two competing models were simulated, a pure drift model (s = 0) based on hypergeometric sampling, identical to the null model used in the Monte Carlo tests; and a selection model where the parental mtDNA pool was adjusted based on a selection coefficient ($s \neq 0$), prior to sampling. Summary statistics for the ABC analysis were calculated on both observed and simulated data and a set of five summary statistics (mean heteroplasmy, mean normalized heteroplasmy shift, median heteroplasmy and 25th and 75th percentiles of heteroplasmy level) were selected for their high information content using a random forest-based approach with the `abcrf` R package. [112] Model choice was performed by training a random forest classifier (abcrf::abcrf) using a reference table generated from 10,000 simulations (5,000 per model), with a forest of 500 trees. The `predict` function was then used to calculate the posterior probability of each model for the observed data based on the proportion of votes from the trees in the forest. For parameter estimation, the posterior distribution of the selection coefficient (s) was estimated for each lineage individually using the "Lenormand" ABC-SMC algorithm [113] implemented in the `EasyABC::ABC_sequential` R package. [114] The analysis was run with 1,500 particles and an adaptive tolerance scheme set by a minimum acceptance rate of 0.02 and alpha = 0.5. Uniform prior of

868 $U[-1, 0.1]$ for the selection coefficient was used. To validate the model's goodness-of-fit, we per-
869 formed a posterior predictive check. For each lineage, we simulated a full dataset using parameters
870 drawn from its posterior distribution and calculated the 95% credible intervals for each of the five
871 summary statistics. The observed summary statistics fell within their corresponding 95% credible in-
872 tervals 94.3% of the time, demonstrating a well-calibrated model. Posterior median estimates and 95%
873 credible intervals were calculated from the accepted particles, and lineages were classified as showing
874 significant selection if the credible interval did not contain zero.
875

Main Figures

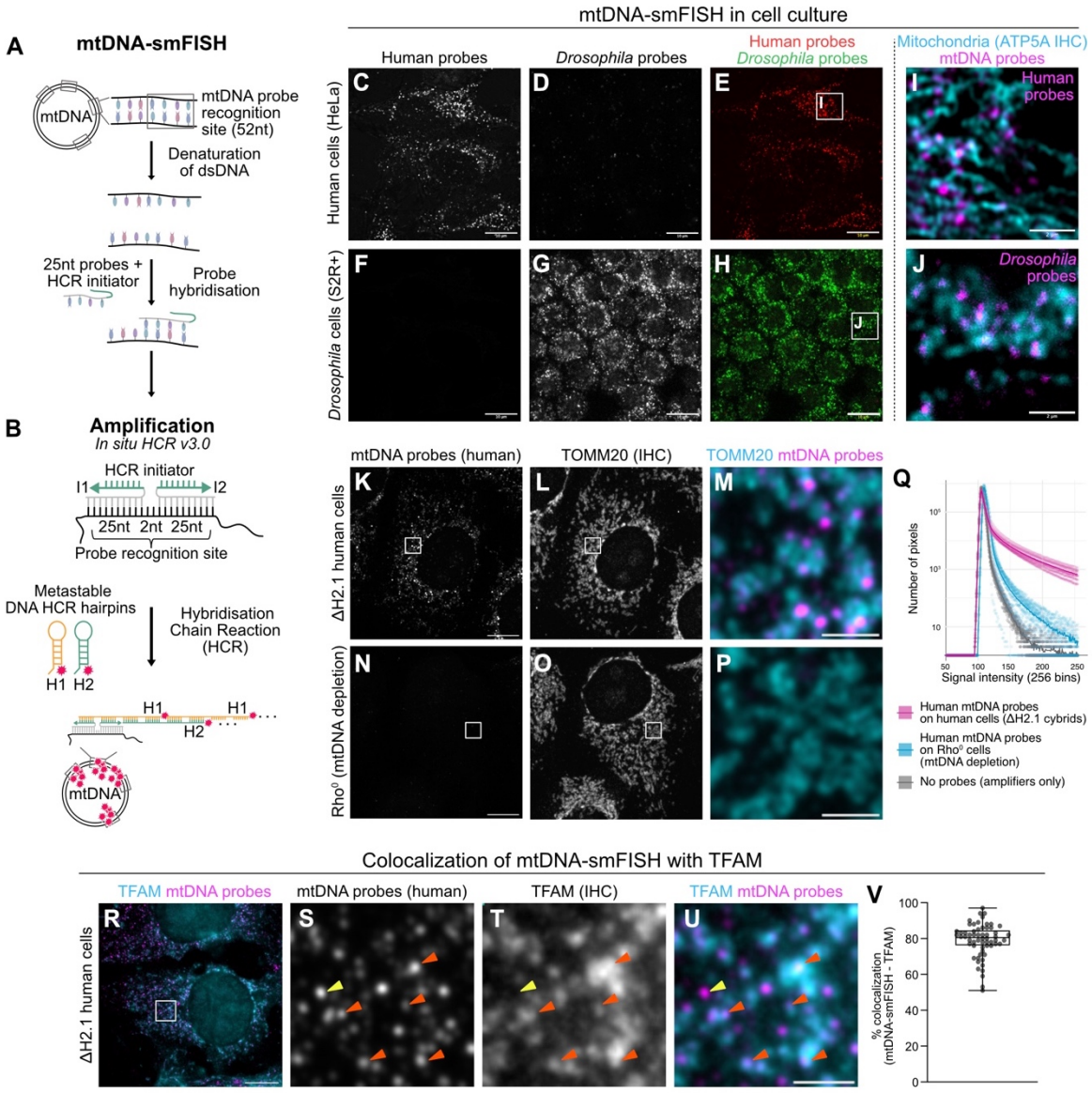


Figure 1: Single-molecule Fluorescent *In situ* hybridisation of mtDNA (mtDNA-smFISH) in cell culture. (**A**) Pairs of 25-nucleotide (nt) probes were designed against 52nt mtDNA target sequences, and used for *in situ* hybridisation after denaturation. (**B**) Signal amplification relied on metastable DNA hairpins recognising an initiator sequence formed when a probe pair hybridises on the target sequence, initiating an enzyme-free hybridisation chain reaction (HCR). (**C-H**) Representative images of mtDNA-smFISH in human HeLa (Airyscan imaging, C-E) or *Drosophila* S2R+ (confocal imaging, F-H) cells with probes against human (C,F,E,H) or *Drosophila* (D,G,E,H) mtDNA. (**I,J**) Zoomed areas boxed in (E,H) showing mtDNA-smFISH (magenta) followed by co-immunostaining (cyan) against the mitochondrial marker ATP5A. (**K-Q**) mtDNA-smFISH (K-P) and signal quantification (Q, Experiment 3 in Figure S2H-J) with probes against human mtDNA and co-immunostaining with the mitochondrial marker TOMM20 in a ΔH2.1 cybrid cell-line (low percentages of deleted mtDNA) (K-M) and the same cell-line with mtDNA depletion (rho^0) upon ddC

treatment (N-P). Zoomed areas boxed in (M,P) show mtDNA-smFISH (magenta) followed by co-immunostaining (cyan) against TOMM20. (**R-U**) mtDNA-smFISH with human mtDNA probes (magenta) with co-immunostaining against the nucleoid marker TFAM (cyan), with higher magnification of boxed region (S-U). Arrowheads illustrate mtDNA-smFISH puncta that colocalize (red) or not (yellow) with TFAM signal. (**V**) Colocalization quantification of human mtDNA probe signal with TFAM staining after masking with TOMM20; 60 cells analysed across three independent experiments. Scale bars are 10µm (C-H,K,N,R), or 2µm (I,J,M,P,U). See also Figure S1,2; Table S1.

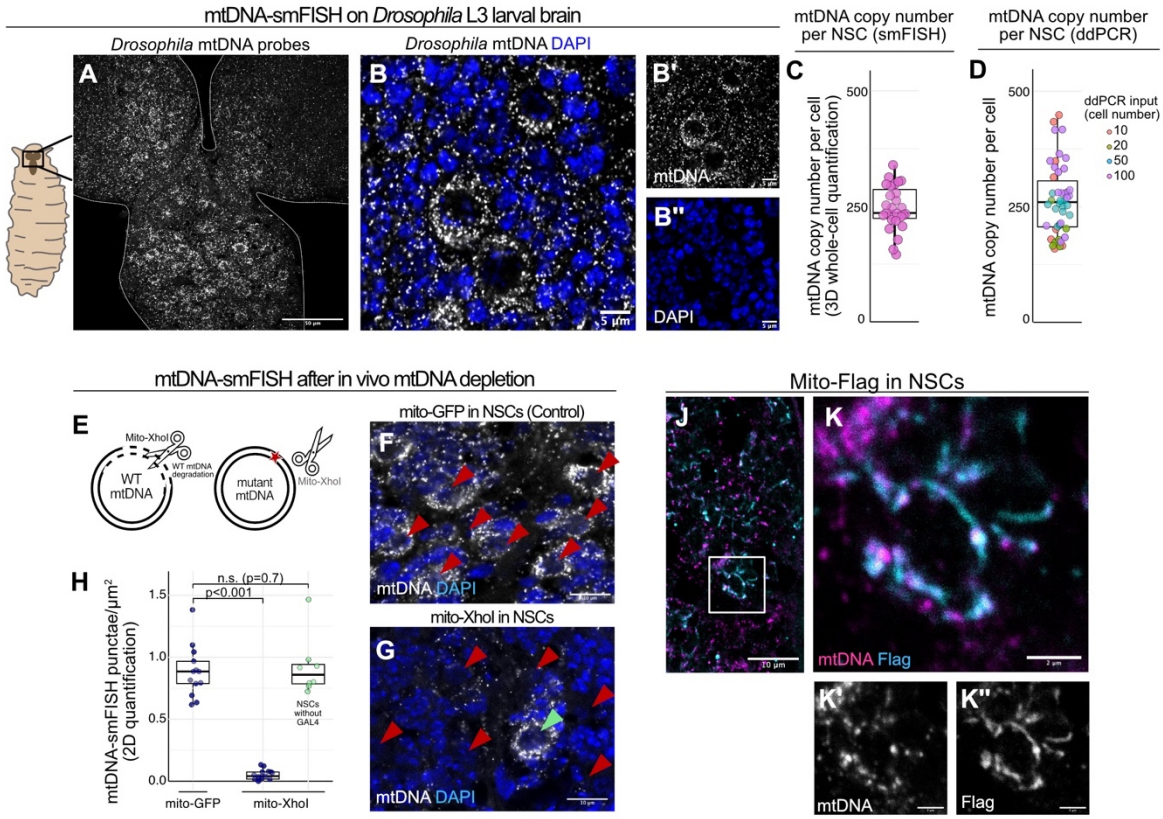


Figure 2: mtDNA-smFISH in whole-mount *Drosophila* tissue. (**A,B**) Representative confocal images of mtDNA-smFISH (gray) in *Drosophila* third instar larva brain and co-labelling with DAPI (blue) to mark nuclei. Single channels of B are in B', B''. (**C,D**) mtDNA CN quantification in complete single NSCs by mtDNA-smFISH across the 3D z-stack (C) or by ddPCR (D), with each dot representing mtDNA CN in a single NSC. (**E**) Schematic of mito-XhoI activity resulting in digestion and degradation of wild-type (WT) but not mutant mtDNA. (**F-H**) Mito-GFP control (F) or mito-XhoI (G) expression in NSCs (Worniu-GAL4) of homoplasmic WT *D. melanogaster* larval brains, followed by mtDNA-smFISH (gray) and DAPI counterstaining (blue). Red arrowheads indicate NSCs; green arrowhead indicates a NSC that does not express Worniu-GAL4 and therefore retains WT mtDNA. Quantification of mtDNA-smFISH puncta in 2D confocal sections of NSCs, presented as puncta per µm^2 (H) (Mann-Whitney U test with Holm-Bonferroni multiple test correction). (**J,K**) mtDNA-smFISH (magenta) and immunostaining (cyan) against Flag in NSCs expressing a

mitochondrial-targeted Flag-tagged transgene. Single channels of K are in K', K''. Scale bars are 50µm (A), 10µm (F,G,J), 5µm (B) or 2µm (K). See also Figure S3,4,5.

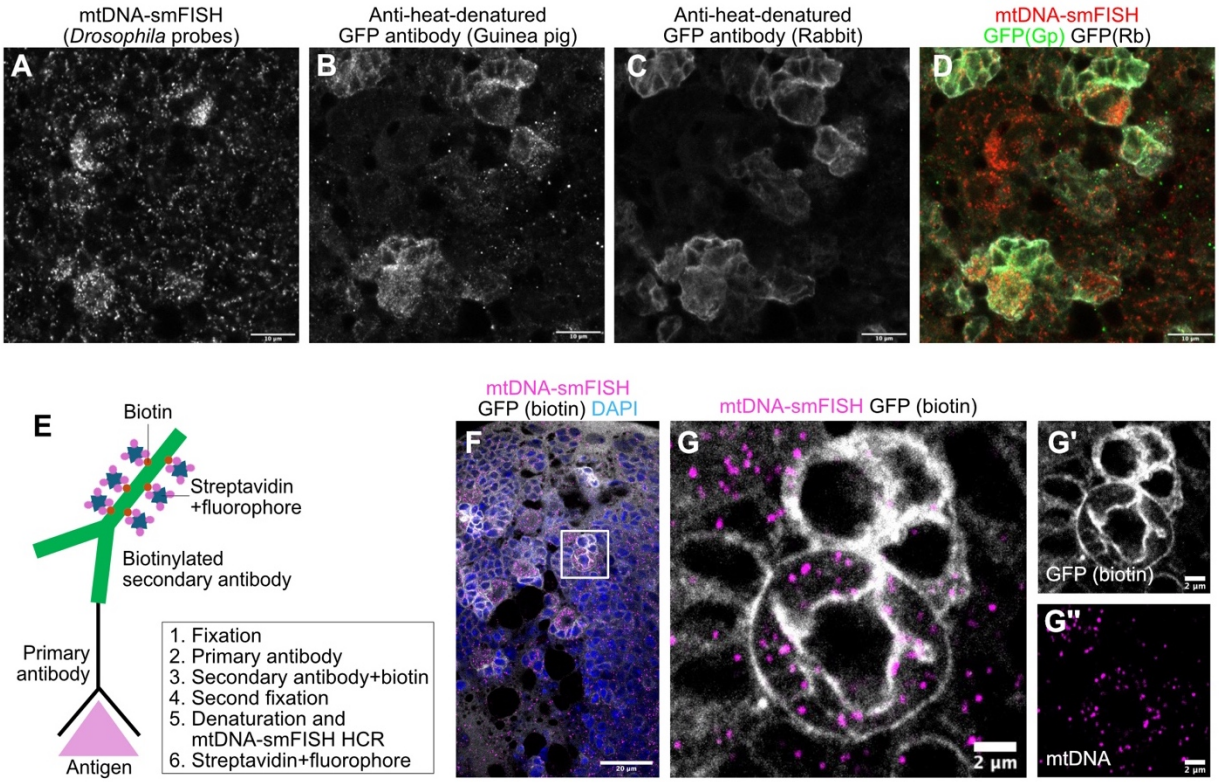


Figure 3: Immunofluorescence combined with mtDNA-smFISH. (**A-D**) Representative confocal images of mtDNA-smFISH (A) with immunostaining using anti-heat denatured GFP antibodies raised in rabbit (B), or guinea pig (C) to mark NSCs (Worniu-GAL4 > UAS-mCD8-GFP) in the *Drosophila* larval brain. (**E**) Schematic of biotin-labelled antibody immunostaining to circumvent denaturation of antigens. (**F,G**) mtDNA-smFISH (magenta) combined with biotin-labelled antibody staining of mCD8-GFP in NSCs (Worniu-GAL4; gray) and DAPI counterstain (blue). Single channels of G are in G', G''. Scale bars are 20µm (F), 10µm (A-D), or 2µm (G-G''). See also Figure S6.

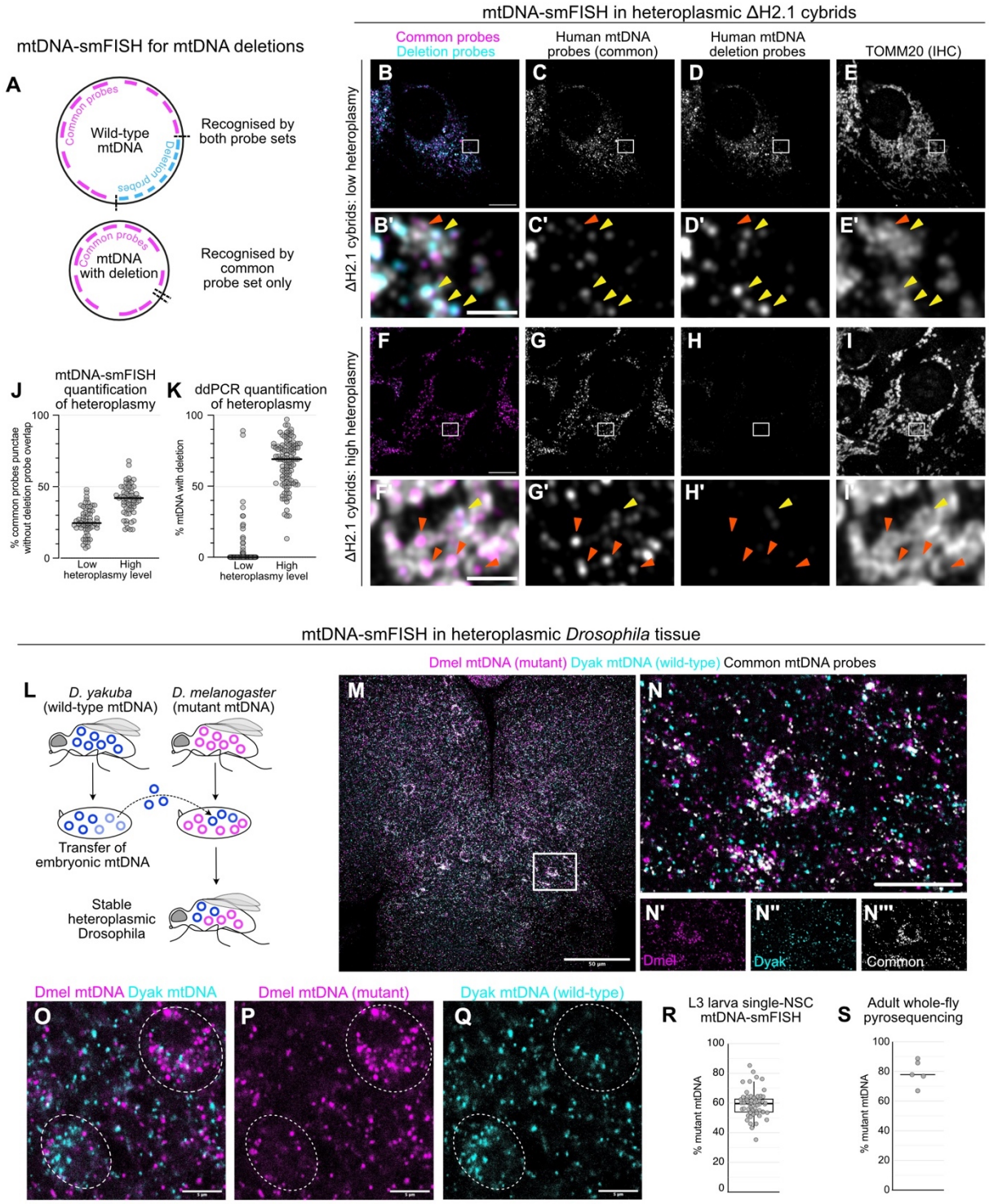


Figure 4: Visualizing heteroplasmy with mtDNA-smFISH. (**A**) Schematic of mtDNA-smFISH for detection of single mtDNA deletions. (**B-I**) Representative confocal images of mtDNA-smFISH in ΔH2.1 cybrid cells with probes against all human mtDNA molecules (magenta, C,G) or only against the deleted region (cyan, D,H), with TOMM2- counterstain (E,I). Note that mtDNA deletion probes only recognize the molecules that do not carry the deletion, and reduced signal indicates higher levels of mutant mtDNA carrying the deletion in a cell. Zooms of regions boxed in (B-I) are shown in (B'-

I'); red arrowheads point to deleted mtDNA; yellow arrowheads to WT mtDNA. (**J,K**) Heteroplasmy levels (% deleted mtDNA) in single ΔH2.1 cybrid cells from low- or high-heteroplasmy clonal cultures, quantified in 2D on maximum-intensity projection after mtDNA-smFISH (J) or by ddPCR (K); 60 cells analysed across three independent experiments. (**L**) Generating heteroplasmic *Drosophila* through mtDNA-transfer between different species. (**M-Q**) mtDNA-smFISH using probes targeting only *D. melanogaster* (mutant, magenta), only *D.yakuba* (WT, cyan) or mtDNA from both species (common, gray) in heteroplasmic *Drosophila* brains. Dashed outlines indicate NSCs. (**R,S**) Heteroplasmy levels (% mutant mtDNA) in single NSCs of L3 larval brains quantified after mtDNA-smFISH (G) or in whole adult flies determined by pyrosequencing (H). Scale bars are 50µm (M), 10µm (N), 5µm (B,F,O-Q) or 2µm (B'.F'). See also Figure S7,8,9,10; Table S1.

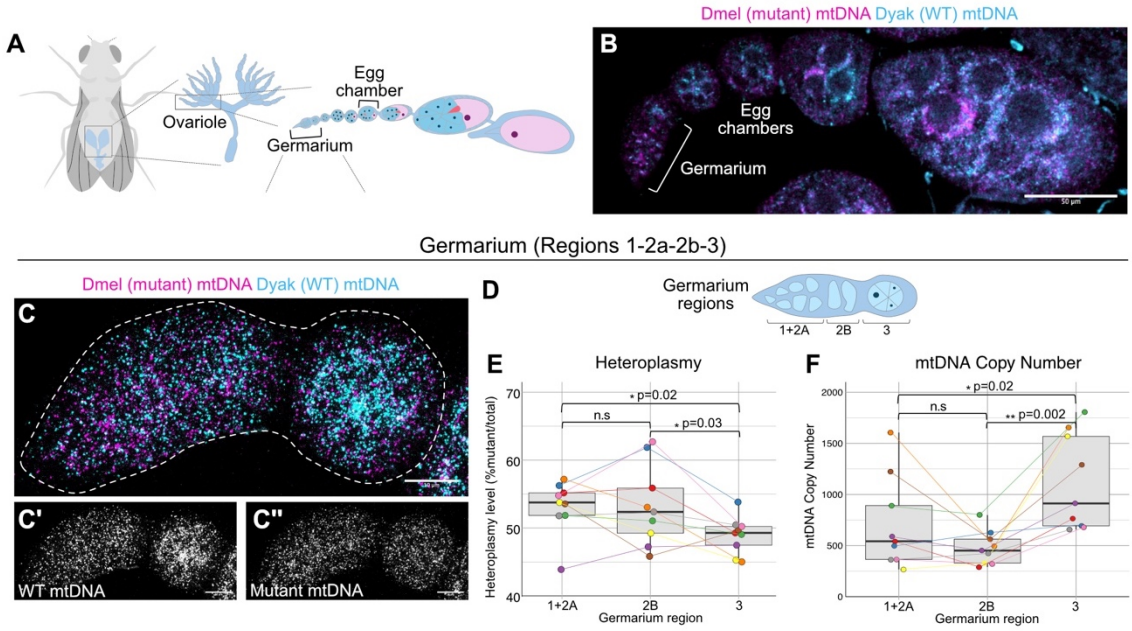
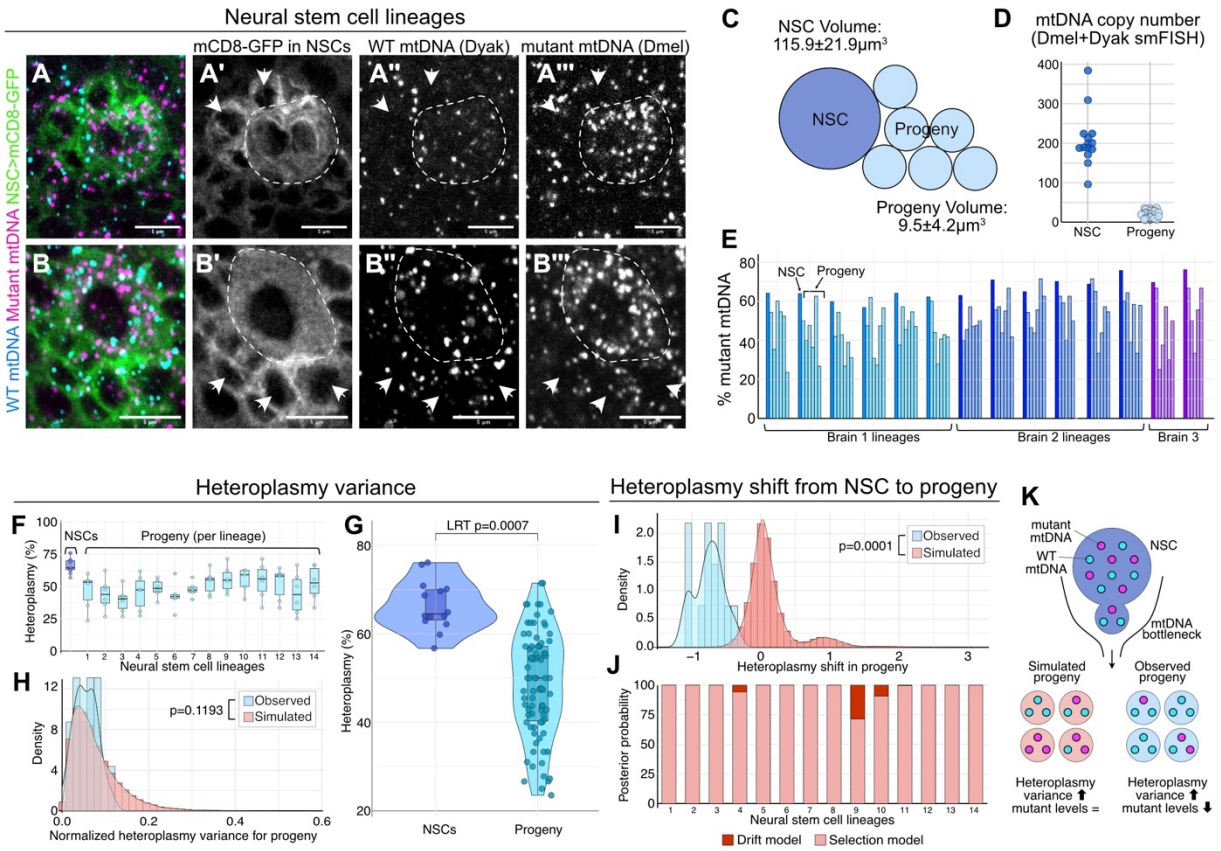


Figure 5: Purifying selection in the *Drosophila* female germline. (**A,B**) Schematic of *Drosophila* oocyte development, with developing oocytes arranged in 15-20 ovarioles, linear arrays of germarium and egg chambers. (**B,C**) Representative confocal images of mtDNA-smFISH using probes targeting only *D. melanogaster* (mutant, magenta, C'') or *D. yakuba* (WT, cyan, C') mtDNA across the germline (B) or the germarium only (C, outline). (**D**) The germarium is divided in three regions that define stages of germ cell development. (**E,F**) Quantification of heteroplasmy level (% mutant mtDNA) (E) and total mtDNA CN (sum of Dmel and Dyak puncta) by mtDNA-smFISH across entire (3D) regions 1+2a, 2b and 3, with dots indicating single germaria (paired t-tests or Wilcoxon signed rank tests). Scale bars are 50µm (B), 10µm (C-C''). See also Figure S11.

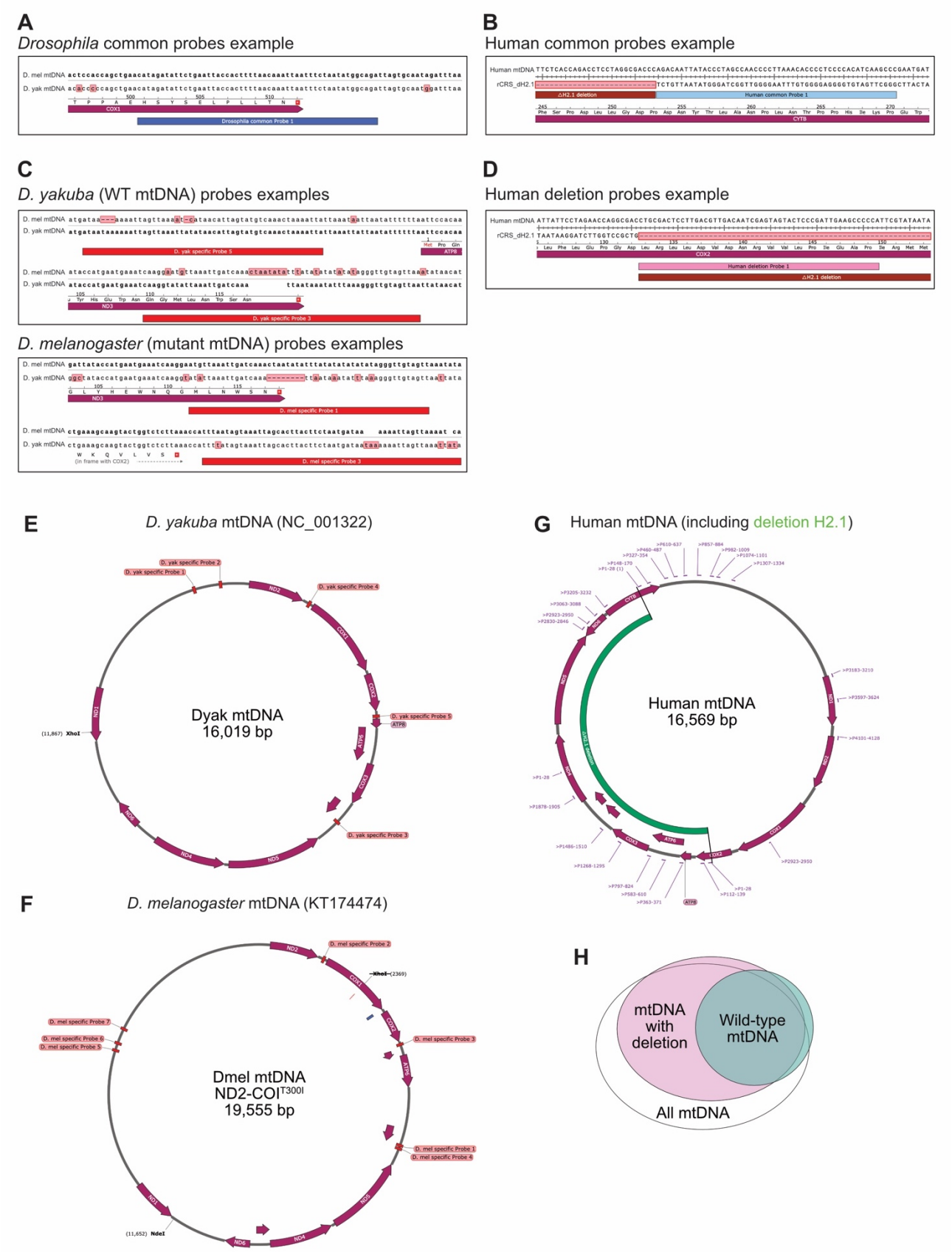


952

953 **Figure 6: Asymmetric mtDNA segregation through a somatic bottleneck during *Drosophila***
954 **neurogenesis.** (**A**) Representative confocal images of NSC lineages expressing Worniu-GAL4 >
955 mCD8-GFP (green,A',B') and mtDNA-smFISH using probes targeting only *D.yakuba* (WT, cyan,
956 A'',B'') or *D. melanogaster* (mutant, magenta, A''',B''') mtDNA. Outline indicates the NSC and
957 arrows point to smaller progeny. Scale bars are 5μm. (**C**) Schematic of *Drosophila* NSC lineage, with
958 NSC volume (dark blue) on average ~12x larger than their differentiating progeny (light blue). (**D**)
959 mtDNA CN in NSCs and their progeny using mtDNA-smFISH. (**E**) Heteroplasmy levels quantified
960 by mtDNA-smFISH in 14 NSC lineages and their youngest-born progeny (identified by Worniu-
961 GAL4 > UAS-mCD8-GFP), across three different brains as indicated. (**F**) Heteroplasmy levels in
962 NSCs pooled across all lineages (dark blue) and their progeny grouped per lineage (light blue). (**G**)
963 Heteroplasmy level distributions across all lineages for NSCs (dark blue) and their progeny cells
964 (light blue). (**H**) Gaussian kernel density estimates of normalized heteroplasmy variance for observed
965 progeny (light blue, n = 14 lineages) and progeny simulated under a random segregation model (red,
966 140,000 simulations). **(I)** Gaussian kernel density estimates of normalized heteroplasmy shift from
967 NSCs to progeny, as observed (light blue, n = 14 lineages) or simulated under a random segregation
968 model (red, 140,000 simulations). (**J**) Posterior probabilities for selection + bottleneck (blue) vs. pure
969 drift (red) models across all 14 lineages (**K**) Model of heteroplasmy segregation through a somatic

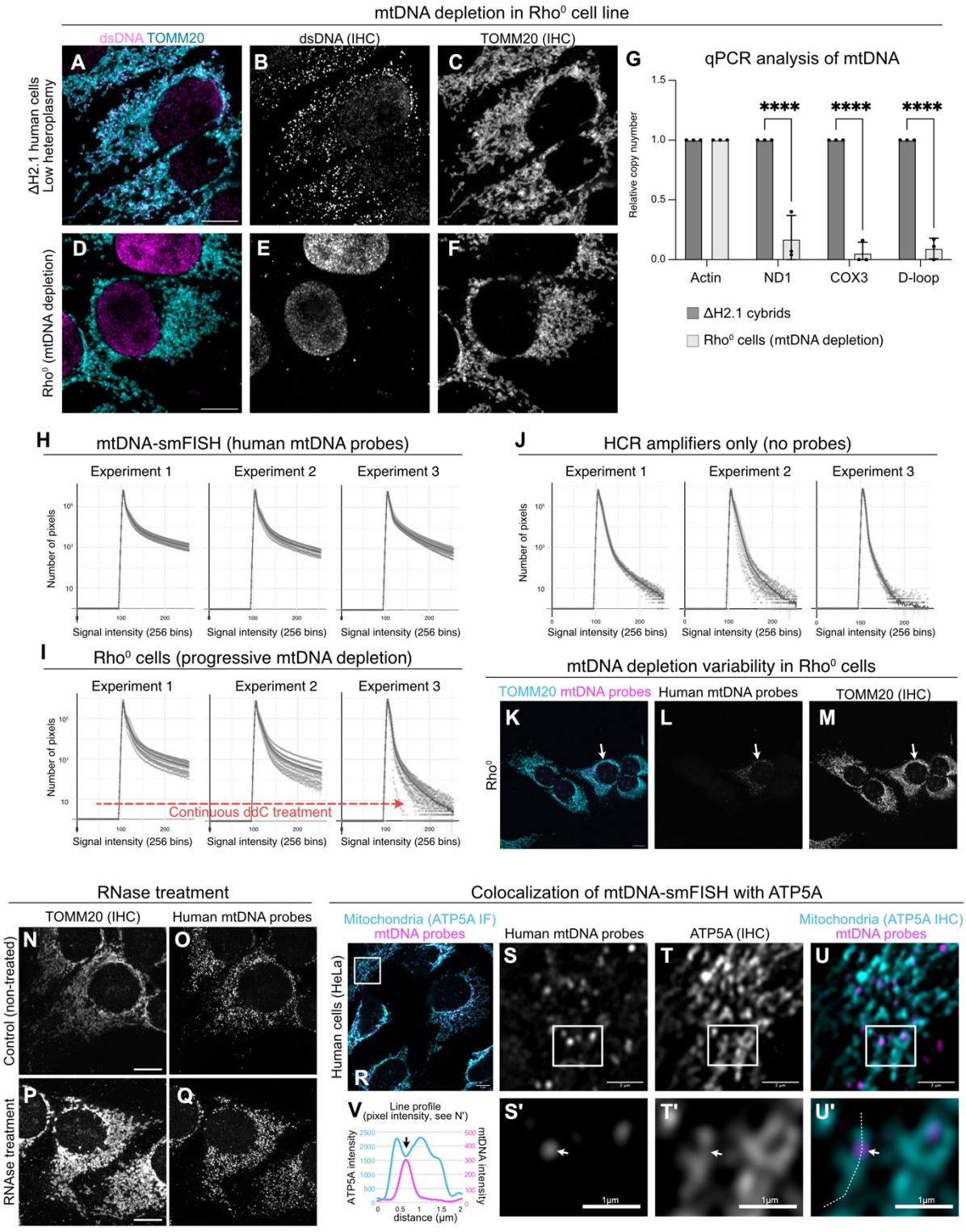
mtDNA bottleneck during asymmetric NSC division, comparing simulated progeny (red) to observed progeny (light blue) as quantified by mtDNA-smFISH. See also Figure S11.

Supplementary figures

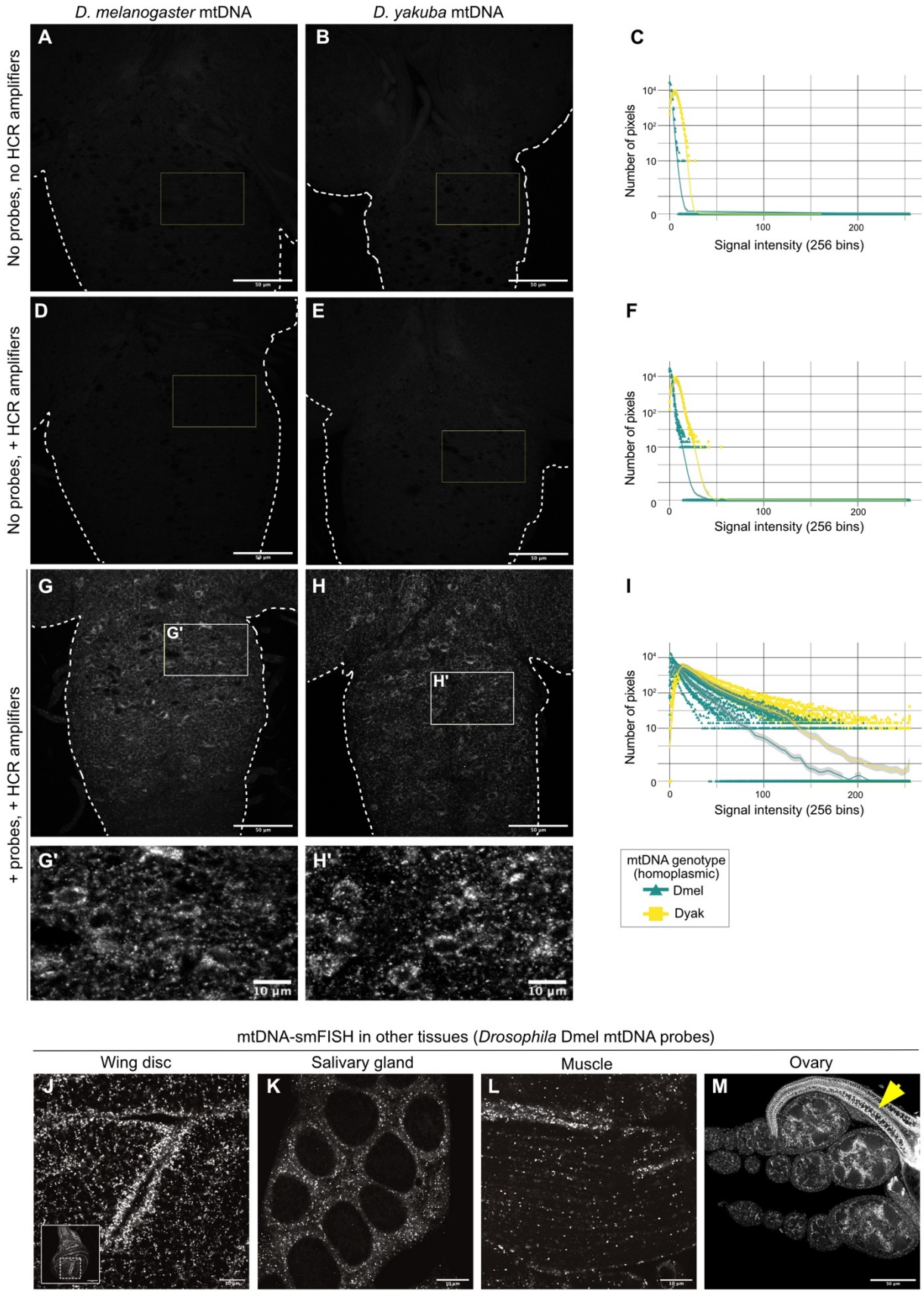


Supplementary Figure 1: Probe Design for mtDNA-smFISH of *Drosophila* and Human mtDNA. (**A-D**) Representative examples of target sequences designed for *Drosophila* mtDNA, common to both *D. melanogaster* and *D. yakuba* (A), specifically for *D. yakuba* (WT, C) or *D. melanogaster*

(mutant, C) mtDNA, or for human mtDNA common to WT and deleted mtDNA (B) or only recognising the WT mtDNA (D). (**E-G**) Schematic of *D. yakuba* (E), and *D. melanogaster* (F) mtDNA and human mtDNA (G) with protein-coding genes in purple and probe target sequences in bright red or pink. Human deleted sequence is indicated in green (G). (**H**) Schematic of how mtDNA-smFISH can distinguish between WT or deleted mtDNA, with deleted molecules only targeted by common mtDNA probes (red) and WT molecules also targeted by deletion-specific probes (green).

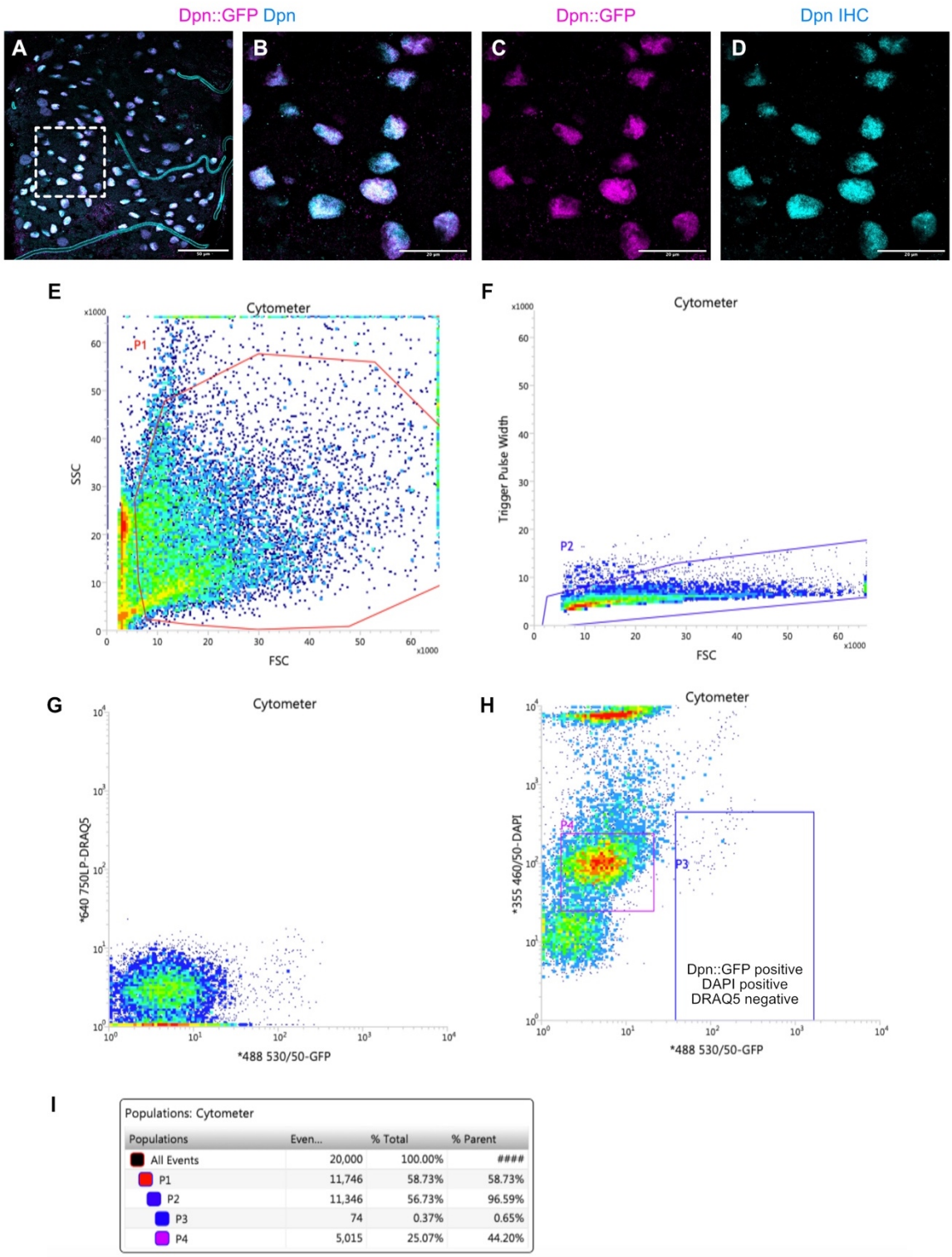


Supplementary Figure 2: mtDNA-smFISH with human mtDNA probes. (**A-F**) Representative confocal images of immunostaining against dsDNA (magenta, B,E) and TOMM20 (cyan, C,F) in a low heteroplasmy ΔH2.1 cybrid cell line (A-C) and a corresponding mtDNA depleted Rho^0 cell line (D-F) generated by ddC treatment. (G) qPCR analysis using ND1, COX3 and D-loop as markers for mtDNA (n = three independent experiments; unpaired t-tests). (**H-J**) mtDNA-smFISH signal (H,I) or background (J, no probes, only HCR amplifiers) quantification in ΔH2.1 cybrid cells upon continuous treatment with control (H) or ddC (I) to generate Rho^0 cells. Experiment 3 is shown in Figure 1Q. (**K-M**) mtDNA-smFISH and TOMM20 co-immunostaining in Rho^0 cells, where some treated cells retain some mtDNA (arrowhead). (**N-Q**) mtDNA-smFISH and TOMM20 co-immunostaining without (N,O) or with (P,Q) prior RNase treatment. (**R-U**) Airyscan imaging of HeLa cells after mtDNA-smFISH with human mtDNA probes (magenta) with co-immunostaining of ATP5A (cyan), with higher magnification of boxed regions (S-U) in (S'-U'). (V) Line profile analysis of signal along the hatched line in U'. Scale bars are 10µm (A,D,K,N,P), 2µm (S-U), 1µm (S'-U').

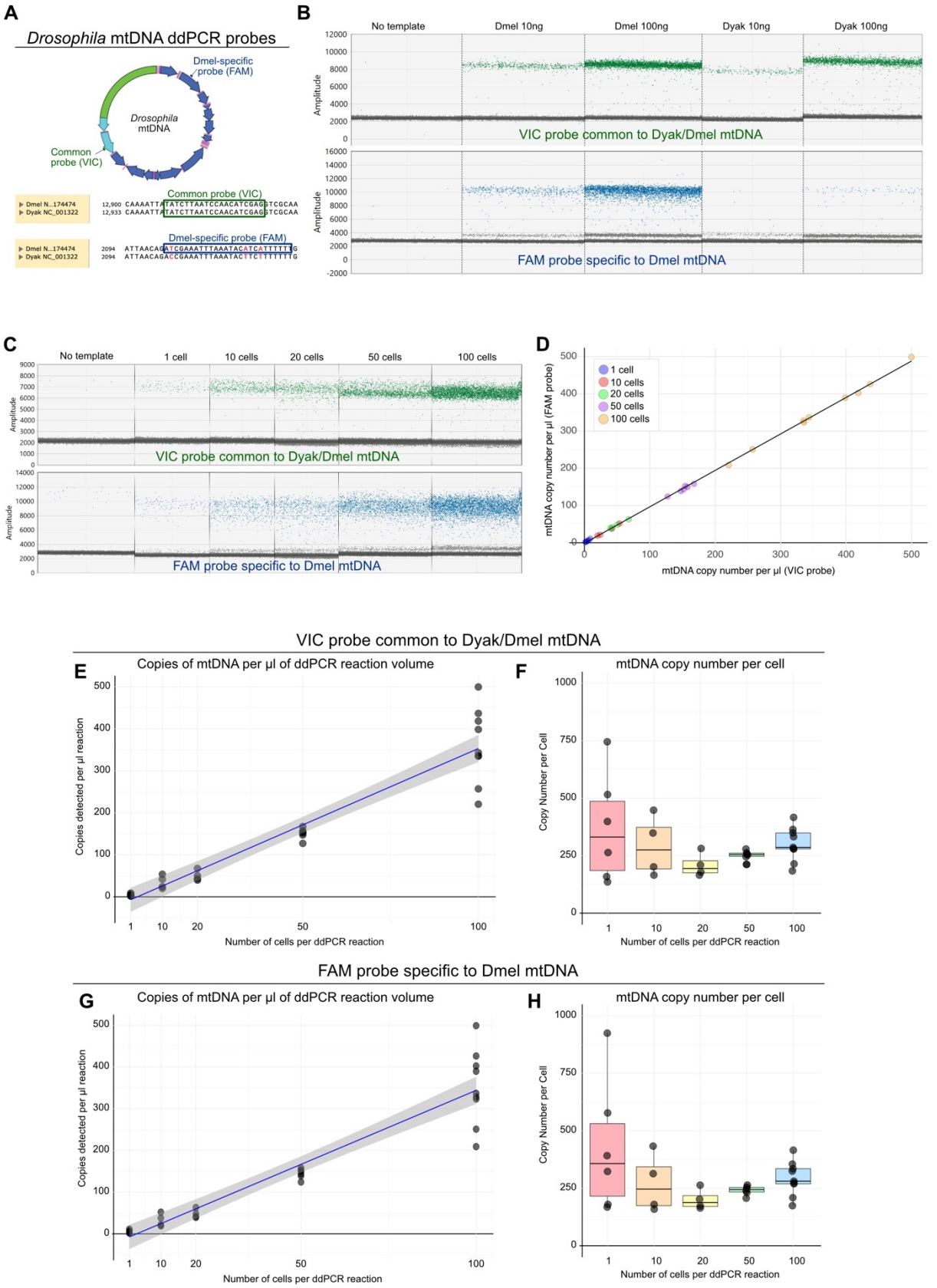


Supplementary Figure 3: mtDNA-smFISH with probes common to *D. melanogaster* and *D. yakuba* mtDNA. (**A-I**) Representative confocal mtDNA-smFISH images (A-H) and signal

quantification (C,F,I) with probes common to both *D. melanogaster* and *D. yakuba* mtDNA in brains of larvae homoplasmic for *D. melanogaster* (A,D,G) or *D. yakuba* (B,E,H) mtDNA, either without probes or amplifiers (A,B,C), without probes (D,E,F), or with both probes and amplifiers added (G,H,I). (G',H') are high magnifications of areas boxed in G,H. (**J-M**) mtDNA-smFISH across various *Drosophila* tissues. Red arrow in (M) points to the dorsal appendage of the maturing egg. Scale bars are 50μm (A,B,D,E,G,H,J-M) or 10μm (G',H').

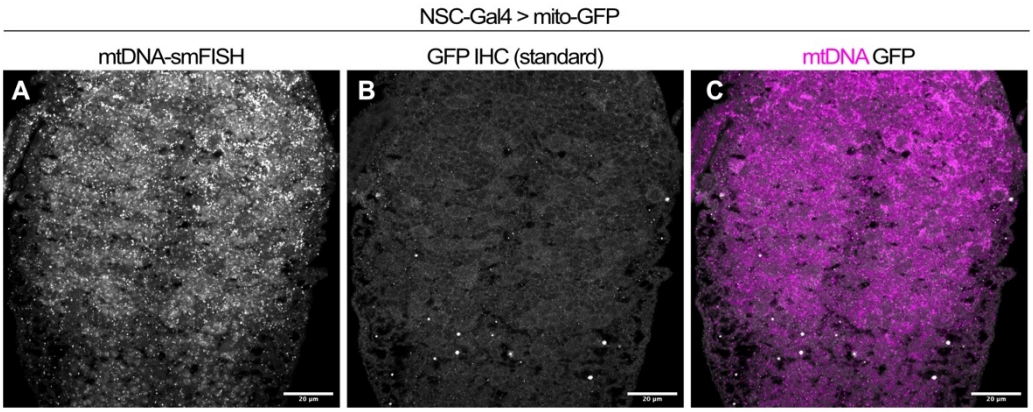


Supplementary Figure 4: FACS-Based Isolation of *Drosophila* NSCs. (**A-D**) Immunostaining of Dpn (cyan) and GFP (magenta) of third instar larval brain from transgenic *Drosophila* with GFP fused to the NSC-marker Dpn (Dpn::GFP). (**E-I**) Representative FACS plots of dissociated third instar larval brains from Dpn::GFP *Drosophila*, with Draq5 and DAPI used to assess viability (G,H), resulting in ~0.37% of all cells retained as NSCs (I).

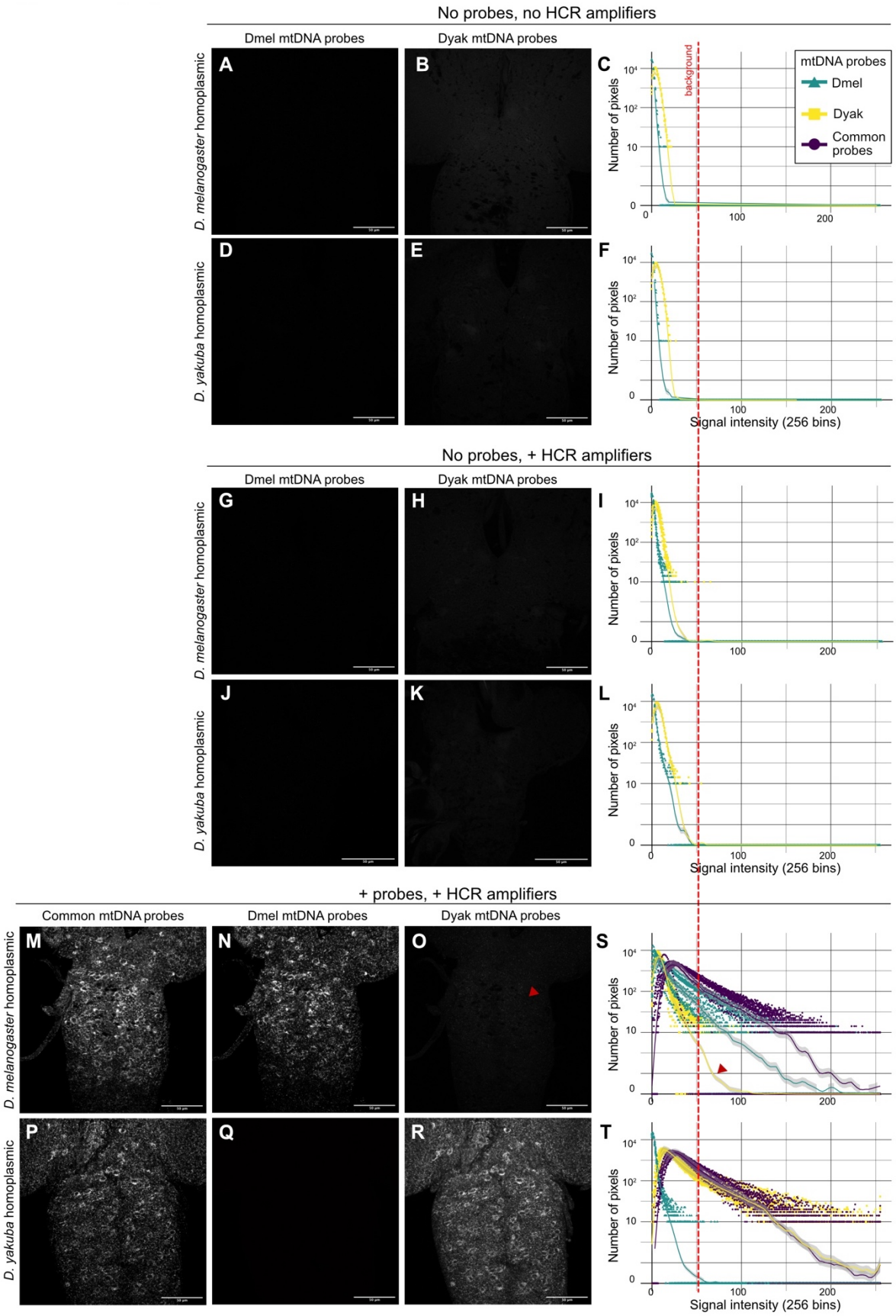


Supplementary Figure 5: Droplet digital PCR (ddPCR) for *Drosophila* mtDNA. (**A**) Schematic representation of VIC and FAM probes for *Drosophila* mtDNA. VIC probe was designed to target both *D. melanogaster* and *D. yakuba* mtDNA. FAM probe was specific to *D. melanogaster* mtDNA.

(**B,C**) ddPCR using VIC (green) and FAM (blue) probes using 0, 10 or 100ng of genomic DNA from homoplasmic *D. melanogaster* or *D. yakuba* (B), or on 1, 10, 20, 50 or 100 sorted NSCs (Dpn::GFP) from homoplasmic *D. melanogaster* (C). (**D**) Correlation between mtDNA CN estimates of VIC and FAM probes on sorted NSCs from homoplasmic *D. melanogaster*. (**E-H**) mtDNA CN measured using VIC probe (E,F) or FAM probe (G,H) on 1, 10, 20, 50 or 100 sorted NSCs from homoplasmic *D. melanogaster*. mtDNA CN increases linearly with increasing cell number (E,G), but larger variability is observed in single-cell samples (F,H).



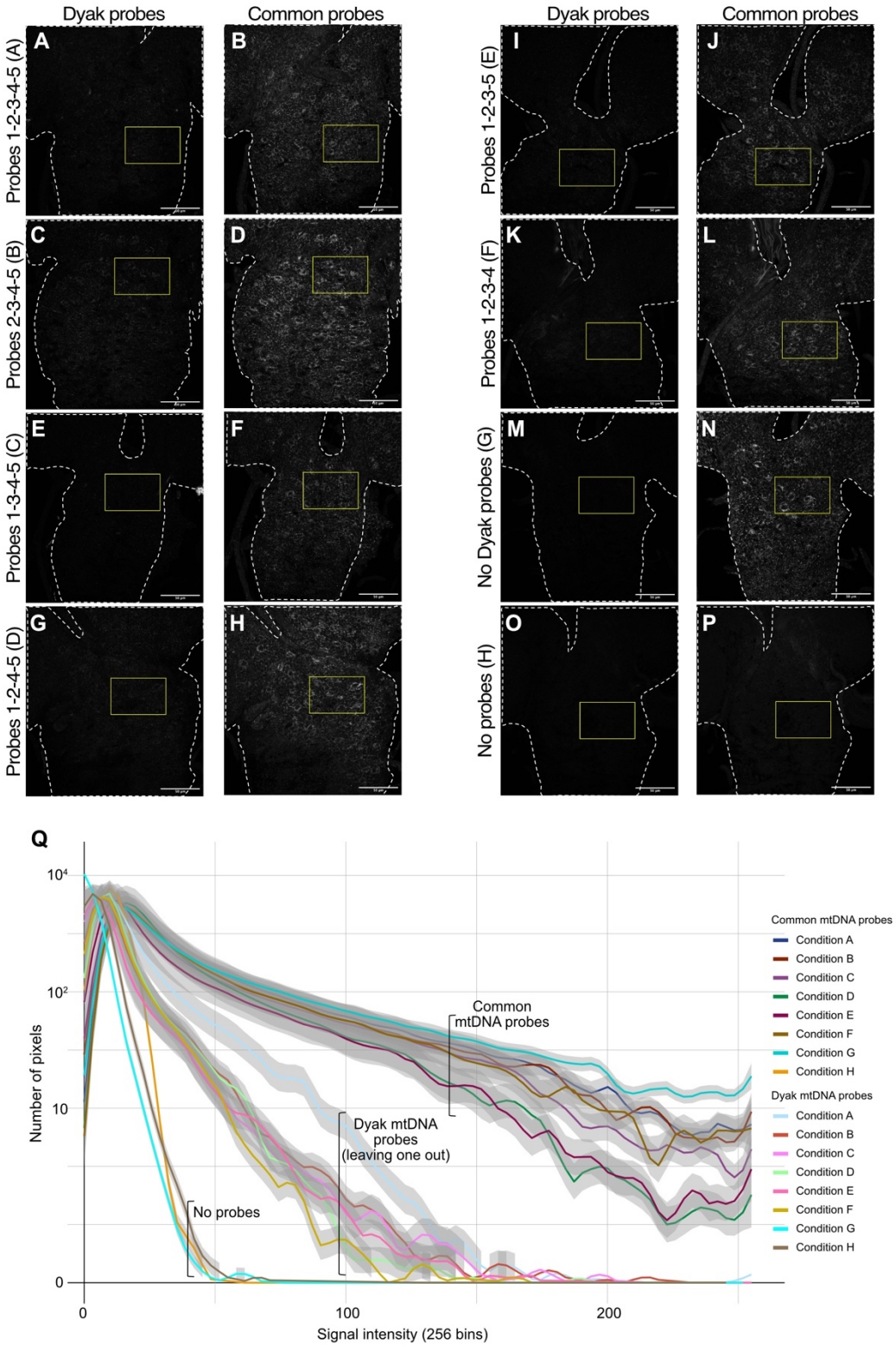
Supplementary Figure 6: Denaturation prevents conventional GFP immunostaining after mtDNA-smFISH. (**A-C**) mtDNA-smFISH (A, magenta) and conventional immunostaining for GFP (Worniu-GAL4 > UAS-mito-GFP) (B, gray) showing no effective GFP staining due to the high denaturation temperature required for mtDNA-smFISH. Scale bars are 50µm.



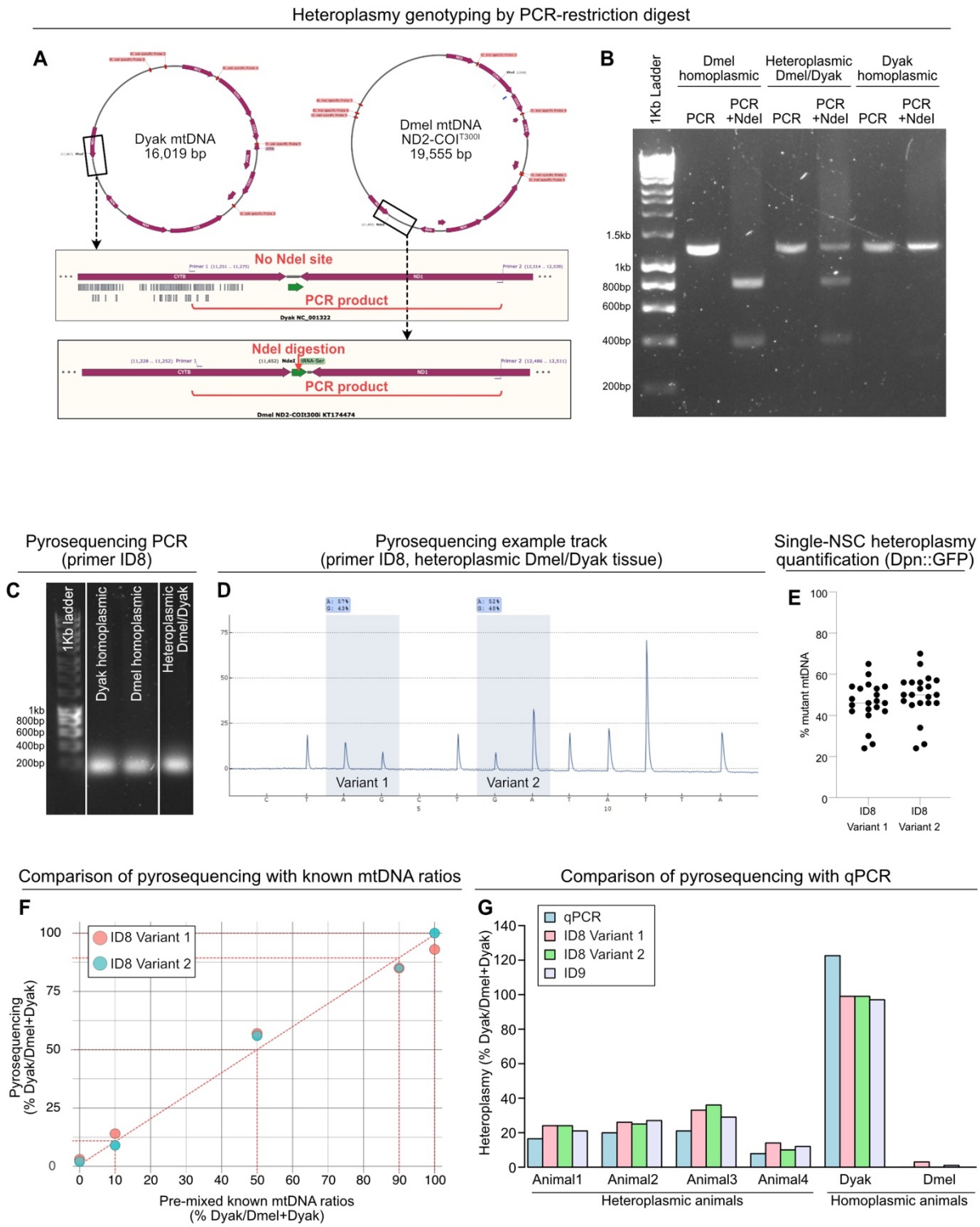
1034

1035 **Supplementary figure 7: Specificity of *D. melanogaster* or *D. yakuba* mtDNA-smFISH.** (**A-T**)
1036 mtDNA-smFISH images (A-E,G-K,M-R) and signal quantification (C,F,I,L,S,T; mean ± s.e.m.) with
1037 probes specific to either *D. melanogaster* (mutant, A,D,G,J,N,Q, green graphs), *D. yakuba*

(B,E,H,K,O,R, yellow graphs) or common to both (M,P, purple graphs) mtDNA in brains of *Drosophila* larvae homoplasmic for *D. melanogaster* (A-C,G-I,M-O) or *D. yakuba* (D-F,J-L,P-R) mtDNA, either without probes or amplifiers (A-F), without probes (G-L), or with both probes and amplifiers added (M-R). Scale bars are 50µm. Red arrowheads indicate a low-level non-specific background from the *D.yakuba* probes in *D.melanogaster* homoplasmic (mutant) background. The red line in the graphs separates true signal from background, with a threshold set at 55 bins.

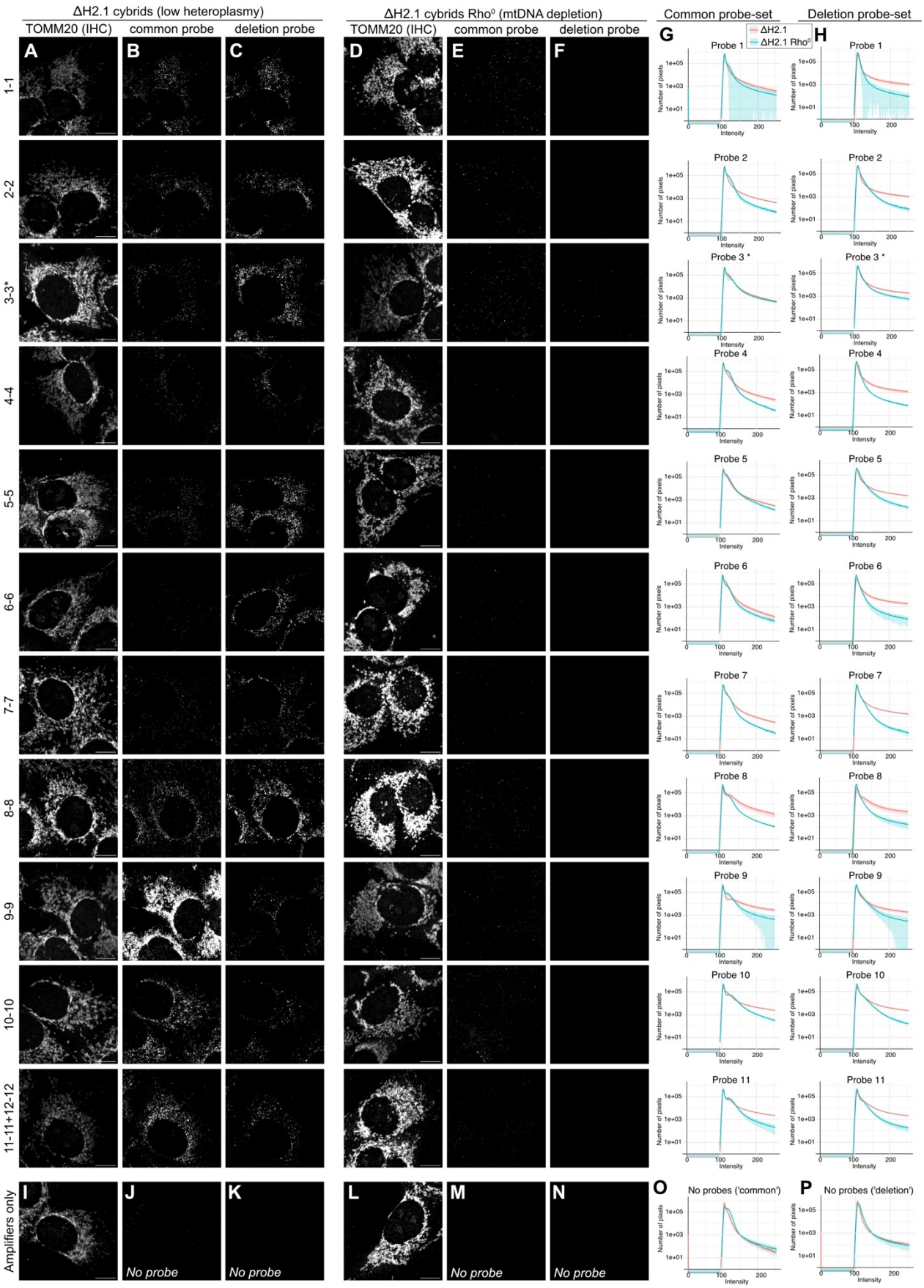


Supplementary Figure 8: Specificity of individual probes for *D. yakuba* mtDNA-smFISH. To assess background of the probe-set specific to *D. yakuba* mtDNA, each of the five individual probe pairs was removed separately from the probe mix used for mtDNA-smFISH on brains from *Drosophila* with homoplasmic *D. melanogaster* mtDNA. Removing individual *D. yakuba* probes (representative confocal images in A,C,E,G,I,K, light colours in Q), all resulted in comparable background levels. mtDNA-smFISH with the common probe set was used as a positive control (representative confocal images in B,D,F,H,J,L, dark colours in Q). No background or signal was observed in absence of *D. yakuba* probes (M,Q) or any probe (O,P,Q). Scale bars are 50μm.



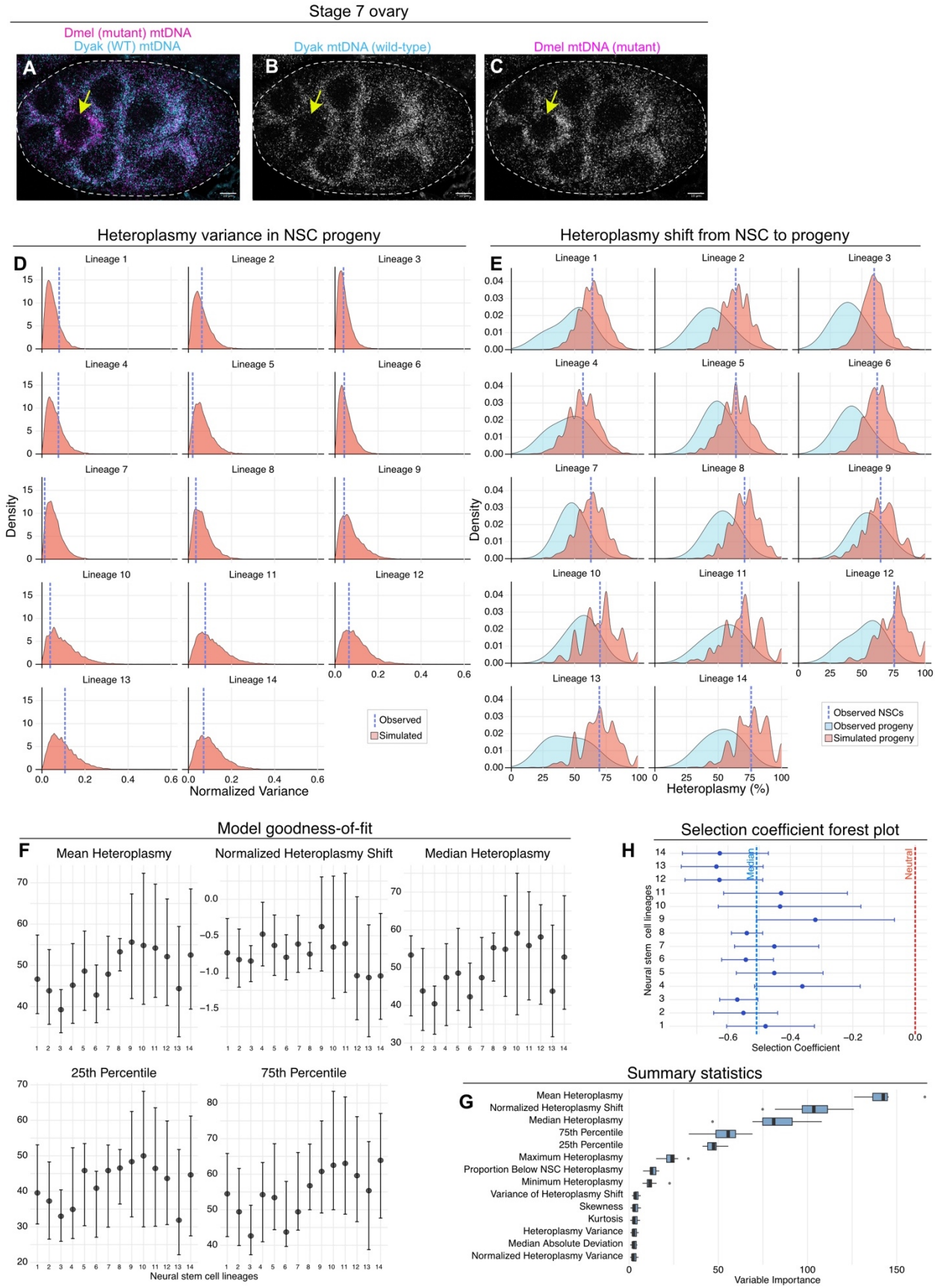
Supplementary figure 9: Heteroplasmy measurement with restriction digestion or pyrosequencing. (**A,B**) Schematic (A) and representative gel image (B) of PCR amplification and NdeI digestion to distinguish *D. yakuba* (WT) from *D. melanogaster* (mutant) mtDNA, with *D. yakuba* lacking the NdeI site. PCR amplification produced a 1284bp (*D. melanogaster*) or 1289bp (*D. yakuba*) product, which, upon digestion with NdeI, resulted in two bands of 425bp and 859bp for the *D. melanogaster* genome only. (**C-G**) Optimisation of pyrosequencing to distinguish *D. yakuba* (WT) from *D. melanogaster* (mutant) mtDNA, using primer pairs ID8 (C-G) or ID9 (G). PCR using primer pair

ID8 amplifies mtDNA from homoplasmic or heteroplasmic *Drosophila* strains with comparable efficiency (C), and allows quantification of heteroplasmy levels using two independent variants in the same PCR fragment (D). Pyrosequencing detects heteroplasmy levels in single NSCs sorted from Dpn::GFP third instar larvae (E). Pyrosequencing detects known ratios of mixed mtDNA from homoplasmic *D. melanogaster* and *D. yakuba* (F), and detects heteroplasmy levels from heteroplasmic or homoplasmic *Drosophila* with comparable accuracy to a previously validated qPCR method [67] (G).



Supplementary figure 10: Specificity of individual human probes for mtDNA-smFISH. (**A-E**) Representative confocal images of mtDNA-smFISH performed on a low heteroplasmy ΔH2.1 cybrid

cell line (A-C, I-K) and a Rho^0 (D-F, L-M) cell line by using single probes for human mtDNA (common, B,E) or human mtDNA with a single deletion (C,F). Co-immunostaining was performed with anti-TOMM20 antibody (A,D,I,L). Each row represents a single probe from each probe set. The last row (I-N) displays very low background given by the amplifiers when no probes are added during hybridization step. Signal quantification is shown in graphs (G,H,O,P). Probe 3 from the common probe set indicated with an * displayed a high background and was removed for further experiments; probe 3 from the deletion probe set was arbitrarily removed from this set as well to keep equal probe numbers. Scale bars are 10μm.



Supplementary Figure 11: Modelling of mtDNA segregation through a somatic bottleneck. (**A-C**) Representative confocal images of mtDNA-smFISH using probes targeting only *D. melanogaster* (mutant, magenta, C) or *D.yakuba* (WT, cyan, B) mtDNA in stage 7 *Drosophila* egg chamber nurse

cells. Arrow indicates a nurse cell with high mutant heteroplasmy level. Scale bars are 10μm. (**D**) Null distributions for normalized heteroplasmy variance from 10,000 random segregation simulations (red density plots) for each lineage. The corresponding observed normalized variance is marked by the dashed blue line. (**E**) Density plots of the observed progeny heteroplasmy (light blue) overlaid on the null distributions from 10,000 random segregation simulations (red) for each lineage. The heteroplasmy of the parent NSC for each lineage is marked by the dashed dark blue line. (**F**) Model goodness-of-fit assessed via posterior predictive check, comparing observed summary statistics (black dots) against 95% credible intervals of posterior predictive distribution (whiskers). (**G**) Random Forest Variable importance of candidate summary statistics for ABC parameter estimation across all 14 lineages, ranked by median importance. (**H**) Selection coefficient estimates for all lineages from Sequential Monte Carlo ABC; Points show posterior median estimates with 95% credible intervals (whiskers); blue dashed line median selection; red dashed line neutral evolution.

Supplementary Table 1: smFISH-mtDNA probe sequences.

References

1. Ludwig, L.S., Lareau, C.A., Ulirsch, J.C., Christian, E., Muus, C., Li, L.H., Pelka, K., Ge, W., Oren, Y., Brack, A., et al. (2019). Lineage Tracing in Humans Enabled by Mitochondrial Mutations and Single-Cell Genomics. Cell.
2. Elliott, H.R., Samuels, D.C., Eden, J.A., Relton, C.L., and Chinnery, P.F. (2008). Pathogenic Mitochondrial DNA Mutations Are Common in the General Population. American Journal of Human Genetics.
3. Wei, W., Keogh, M.J., Wilson, I., Coxhead, J., Ryan, S., Rollinson, S., Griffin, H., Kurzawa-Akanbi, M., Santibanez-Koref, M., Talbot, K., et al. (2017). Mitochondrial DNA point mutations and relative copy number in 1363 disease and control human brains. Acta neuropathologica communications.
4. An, J., Nam, C.H., Kim, R., Lee, Y., Won, H., Park, S., Lee, W.H., Park, H., Yoon, C.J., An, Y., et al. (2024). Mitochondrial DNA mosaicism in normal human somatic cells. Nat Genet *56*, 1665-1677. 10.1038/s41588-024-01838-z.
5. Green, A.P., Klimm, F., Marshall, A.S., Leetmaa, R., Aryaman, J., Gómez-Durán, A., Chinnery, P.F., and Jones, N.S. (2025). Cryptic mitochondrial DNA mutations coincide with mid-late life and are pathophysiologically informative in single cells across tissues and species. Nature Communications *16*, 2250. 10.1038/s41467-025-57286-8.
6. Korotkevich, E., Conrad, D.N., Gartner, Z.J., and O'Farrell, P.H. (2025). Selfish mutations promote age-associated erosion of mtDNA integrity in mammals. Nat Commun *16*, 5435. 10.1038/s41467-025-60477-y.
7. Glynos, A., Bozhilova, L.V., Frison, M., Burr, S., Stewart, J.B., and Chinnery, P.F. (2023). High-throughput single-cell analysis reveals progressive mitochondrial DNA mosaicism throughout life. Science advances.
8. Lareau, C.A., Ludwig, L.S., Muus, C., Gohil, S.H., Zhao, T., Chiang, Z., Pelka, K., Verboon, J.M., Luo, W., Christian, E., et al. (2020). Massively parallel single-cell mitochondrial DNA genotyping and chromatin profiling. Nature Biotechnology.
9. Chinnery, P.F., and Samuels, D.C. (1999). Relaxed Replication of mtDNA: A Model with Implications for the Expression of Disease. Am. J. Hum. Genet.
10. Chinnery, P.F., Howell, N., Lightowlers, R.N., and Turnbull, D.M. (1997). Molecular pathology of MELAS and MERRF. The relationship between mutation load and clinical phenotypes. Brain.
11. Van den Ameele, J., Li, A.Y.Z., Ma, H., and Chinnery, P.F. (2020). Mitochondrial heteroplasmy beyond the oocyte bottleneck. Seminars in Cell and Developmental Biology.
12. Burr, S.P., and Chinnery, P.F. (2024). Origins of tissue and cell-type specificity in mitochondrial DNA (mtDNA) disease. Hum Mol Genet *33*, R3-r11. 10.1093/hmg/ddae059.
13. Gorman, G.S., Schaefer, A.M., Ng, Y., Gomez, N., Blakely, E.L., Alston, C.L., Feeney, C., Horvath, R., Yu-Wai-Man, P., Chinnery, P.F., et al. (2015). Prevalence of nuclear and mitochondrial DNA mutations related to adult mitochondrial disease. Annals of Neurology.
14. Corral-Debrinski, M., Horton, T., Lott, M.T., Shoffner, J.M., McKee, A.C., Beal, M.F., Graham, B.H., and Wallace, D.C. (1994). Marked changes in mitochondrial dna deletion levels in alzheimer brains. Genomics.
15. Bender, A., Krishnan, K.J., Morris, C.M., Taylor, G.A., Reeve, A.K., Perry, R.H., Jaros, E., Hersheson, J.S., Betts, J., Klopstock, T., et al. (2006). High levels of mitochondrial DNA deletions in substantia nigra neurons in aging and Parkinson disease. Nature Genetics.
16. Yuan, Y., Ju, Y.S., Kim, Y., Li, J., Wang, Y., Yoon, C.J., Yang, Y., Martincorena, I., Creighton, C.J., Weinstein, J.N., et al. (2020). Comprehensive molecular characterization of mitochondrial genomes in human cancers. Nature Genetics.

17. Kandul, N.P., Zhang, T., Hay, B.A., and Guo, M. (2016). Selective removal of deletion-bearing mitochondrial DNA in heteroplasmic Drosophila. Nature Communications.
18. Ma, H., and O'Farrell, P.H. (2016). Selfish drive can trump function when animal mitochondrial genomes compete. Nature Genetics.
19. Tsai, P.-I., Korotkevich, E., and O'Farrell, P.H. (2022). Mitigation of age-dependent accumulation of defective mitochondrial genomes. Proceedings of the National Academy of Sciences of the United States of America.
20. Van Den Ameele, J., and Brand, A.H. (2019). Neural stem cell temporal patterning and brain tumour growth rely on oxidative phosphorylation. eLife.
21. Cagin, U., Duncan, O.F., Gatt, A.P., Dionne, M.S., Sweeney, S.T., and Bateman, J.M. (2015). Mitochondrial retrograde signaling regulates neuronal function. Proceedings of the National Academy of Sciences of the United States of America.
22. Tsuyama, T., Tsubouchi, A., Usui, T., Imamura, H., and Uemura, T. (2017). Mitochondrial dysfunction induces dendritic loss via eIF2α phosphorylation. The Journal of cell biology.
23. Andreazza, S., Samstag, C.L., Sanchez-Martinez, A., Fernandez-Vizarra, E., Gomez-Duran, A., Lee, J.J., Tufi, R., Hipp, M.J., Schmidt, E.K., Nicholls, T.J., et al. (2019). Mitochondrially-targeted APOBEC1 is a potent mtDNA mutator affecting mitochondrial function and organismal fitness in Drosophila. Nature Communications.
24. Chen, Z., Qi, Y., French, S., Zhang, G., Garcia, R.C., Balaban, R., and Xu, H. (2015). Genetic mosaic analysis of a deleterious mitochondrial DNA mutation in Drosophila reveals novel aspects of mitochondrial regulation and function. Molecular Biology of the Cell.
25. Petridi, S., Dubal, D., Rikhy, R., and van den Ameele, J. (2022). Mitochondrial respiration and dynamics of in vivo neural stem cells. Development.
26. Zhang, H., Burr, S.P., and Chinnery, P.F. (2018). The mitochondrial DNA genetic bottleneck: inheritance and beyond. Essays Biochem *62*, 225-234. 10.1042/ebc20170096.
27. Floros, V.I., Pyle, A., Dietmann, S., Wei, W., Tang, W.W.C., Irie, N., Payne, B., Capalbo, A., Noli, L., and Coxhead, J. (2018). Segregation of mitochondrial DNA heteroplasmy through a developmental genetic bottleneck in human embryos. Nature cell biology. Nature Publishing Group.
28. Wei, W., Wei, W., Tuna, S., Tuna, S., Keogh, M.J., Smith, K.G.C.K.R.K.G.C., Aitman, T.J., Aitman, T.J., Beales, P.L., Beales, P.L., et al. (2019). Germline selection shapes human mitochondrial DNA diversity. Science.
29. Olivo, P.D., Van de Walle, M.J., Laipis, P.J., and Hauswirth, W.W. (1983). Nucleotide sequence evidence for rapid genotypic shifts in the bovine mitochondrial DNA D-loop. Nature *306*, 400-402. 10.1038/306400a0.
30. Jenuth, J.P., Peterson, A.C., Fu, K., and Shoubridge, E.A. (1996). Random genetic drift in the female germline explains the rapid segregation of mammalian mitochondrial DNA. Nature genetics. Nature Publishing Group.
31. Hurd, T.R., Herrmann, B., Sauerwald, J., Sanny, J., Grosch, M., and Lehmann, R. (2016). Long Oskar Controls Mitochondrial Inheritance in Drosophila melanogaster. Dev Cell *39*, 560-571. 10.1016/j.devcel.2016.11.004.
32. Barrett, A., Arbeithuber, B., Zaidi, A., Wilton, P., Paul, I.M., Nielsen, R., and Makova, K.D. (2020). Pronounced somatic bottleneck in mitochondrial DNA of human hair. Philos Trans R Soc Lond B Biol Sci *375*, 20190175. 10.1098/rstb.2019.0175.
33. Bendall, K.E., Macaulay, V.A., and Sykes, B.C. (1997). Variable Levels of a Heteroplasmic Point Mutation in Individual Hair Roots. The American Journal of Human Genetics *61*, 1303-1308. 10.1086/301636.
34. Sekiguchi, K., Imaizumi, K., Matsuda, H., Mizuno, N., Yoshida, K., Senju, H., Sato, H., and Kasai, K. (2003). MtDNA Sequence Analysis Using Capillary Electrophoresis and Its

Application to the Analysis of MtDNA in Hair. Japanese journal of science and technology for identification *7*, 123-130. 10.3408/jasti.7.123.
35. Lechuga-Vieco, A.V., Latorre-Pellicer, A., Johnston, I.G., Prota, G., Gileadi, U., Justo-Méndez, R., Acín-Pérez, R., Martínez-De-Mena, R., Fernández-Toro, J.M., Jimenez-Blasco, D., et al. (2020). Cell identity and nucleo-mitochondrial genetic context modulate OXPHOS performance and determine somatic heteroplasmy dynamics. Science Advances. American Association for the Advancement of Science.
36. Lareau, C.A., Dubois, S.M., Buquicchio, F.A., Hsieh, Y.H., Garg, K., Kautz, P., Nitsch, L., Praktiknjo, S.D., Maschmeyer, P., Verboon, J.M., et al. (2023). Single-cell multi-omics of mitochondrial DNA disorders reveals dynamics of purifying selection across human immune cells. Nature Genetics.
37. Lareau, C.A., Liu, V., Muus, C., Praktiknjo, S.D., Nitsch, L., Kautz, P., Sandor, K., Yin, Y., Gutierrez, J.C., Pelka, K., et al. (2023). Mitochondrial single-cell ATAC-seq for high-throughput multi-omic detection of mitochondrial genotypes and chromatin accessibility. Nature Protocols.
38. Walker, M.A., Lareau, C.A., Ludwig, L.S., Karaa, A., Sankaran, V.G., Regev, A., and Mootha, V.K. (2020). Purifying Selection against Pathogenic Mitochondrial DNA in Human T Cells. New England Journal of Medicine.
39. Lieber, T., Jeedigunta, S.P., Palozzi, J.M., Lehmann, R., and Hurd, T.R. (2019). Mitochondrial fragmentation drives selective removal of deleterious mtDNA in the germline. Nature.
40. Gilkerson, R.W., Schon, E.A., Hernandez, E., and Davidson, M.M. (2008). Mitochondrial nucleoids maintain genetic autonomy but allow for functional complementation. J Cell Biol *181*, 1117-1128. 10.1083/jcb.200712101.
41. Zhang, C., Chen, Z., Ma, H., and Xu, H. (2025). Replication competition drives the selective mtDNA inheritance in Drosophila ovary. Cell Rep *44*, 116221. 10.1016/j.celrep.2025.116221.
42. Chatre, L., and Ricchetti, M. (2021). mTRIP, an Imaging Tool to Investigate Mitochondrial DNA Dynamics in Physiology and Disease at the Single-Cell Resolution. Methods Mol Biol *2275*, 247-263. 10.1007/978-1-0716-1262-0_15.
43. Zhang, K., Deng, R., Teng, X., Li, Y., Sun, Y., Ren, X., and Li, J. (2018). Direct Visualization of Single-Nucleotide Variation in mtDNA Using a CRISPR/Cas9-Mediated Proximity Ligation Assay. J Am Chem Soc *140*, 11293-11301. 10.1021/jacs.8b05309.
44. Larsson, C., Koch, J., Nygren, A., Janssen, G., Raap, A.K., Landegren, U., and Nilsson, M. (2004). In situ genotyping individual DNA molecules by target-primed rolling-circle amplification of padlock probes. Nature Methods.
45. Roussou, R., Metzler, D., Padovani, F., Thoma, F., Schwarz, R., Shraiman, B., Schmoller, K.M., and Osman, C. (2024). Real-time assessment of mitochondrial DNA heteroplasmy dynamics at the single-cell level. The EMBO Journal, 1-20-20. https://doi.org/10.1038/s44318-024-00183-5.
46. Prole, D.L., Chinnery, P.F., and Jones, N.S. (2020). Visualizing, quantifying, and manipulating mitochondrial DNA in vivo. Journal of Biological Chemistry.
47. Choi, H.M.T., Schwarzkopf, M., Fornace, M.E., Acharya, A., Artavanis, G., Stegmaier, J., Cunha, A., and Pierce, N.A. (2018). Third-generation in situ hybridization chain reaction: Multiplexed, quantitative, sensitive, versatile, robust. Development (Cambridge).
48. Choi, H.M., Chang, J.Y., Trinh le, A., Padilla, J.E., Fraser, S.E., and Pierce, N.A. (2010). Programmable in situ amplification for multiplexed imaging of mRNA expression. Nat Biotechnol *28*, 1208-1212. 10.1038/nbt.1692.

49. Choi, H.M., Beck, V.A., and Pierce, N.A. (2014). Next-generation in situ hybridization chain reaction: higher gain, lower cost, greater durability. ACS Nano *8*, 4284-4294. 10.1021/nn405717p.
50. Olivares-Abril, J., Joha, J., Lee, J.Y., and Davis, I. (2024). Optimization of hybridization chain reaction for imaging single RNA molecules in Drosophila larvae. Fly (Austin) *18*, 2409968. 10.1080/19336934.2024.2409968.
51. Kent, S.P., Ryan, K.H., and Siegel, A.L. (1978). Steric hindrance as a factor in the reaction of labeled antibody with cell surface antigenic determinants. J Histochem Cytochem *26*, 618-621. 10.1177/26.8.357645.
52. Zhang, C., Chen, J., Sun, R., Huang, Z., Luo, Z., Zhou, C., Wu, M., Duan, Y., and Li, Y. (2020). The Recent Development of Hybridization Chain Reaction Strategies in Biosensors. ACS Sens *5*, 2977-3000. 10.1021/acssensors.0c01453.
53. Stephan, T., Roesch, A., Riedel, D., and Jakobs, S. (2019). Live-cell STED nanoscopy of mitochondrial cristae. Sci Rep *9*, 12419. 10.1038/s41598-019-48838-2.
54. Chen, Z., Wang, Z.H., Zhang, G., Bleck, C.K.E., Chung, D.J., Madison, G.P., Lindberg, E., Combs, C., Balaban, R.S., and Xu, H. (2020). Mitochondrial DNA segregation and replication restrict the transmission of detrimental mutation. J Cell Biol *219*. 10.1083/jcb.201905160.
55. Jakubke, C., Roussou, R., Maiser, A., Schug, C., Thoma, F., Bunk, D., Hörl, D., Leonhardt, H., Walter, P., Klecker, T., and Osman, C. (2021). Cristae-dependent quality control of the mitochondrial genome. Sci Adv *7*, eabi8886. 10.1126/sciadv.abi8886.
56. Ekstrand, M.I., Falkenberg, M., Rantanen, A., Park, C.B., Gaspari, M., Hultenby, K., Rustin, P., Gustafsson, C.M., and Larsson, N.G. (2004). Mitochondrial transcription factor A regulates mtDNA copy number in mammals. Human Molecular Genetics.
57. Isaac, R.S., Tullius, T.W., Hansen, K.G., Dubocanin, D., Couvillion, M., Stergachis, A.B., and Churchman, L.S. (2024). Single-nucleoid architecture reveals heterogeneous packaging of mitochondrial DNA. Nat Struct Mol Biol *31*, 568-577. 10.1038/s41594-024-01225-6.
58. Kukat, C., Davies, K.M., Wurm, C.A., Spåhr, H., Bonekamp, N.A., Kühl, I., Joos, F., Polosa, P.L., Park, C.B., Posse, V., et al. (2015). Cross-strand binding of TFAM to a single mtDNA molecule forms the mitochondrial nucleoid. Proceedings of the National Academy of Sciences.
59. Brand, A.H., and Perrimon, N. (1993). Targeted gene expression as a means of altering cell fates and generating dominant phenotypes. Development (Cambridge, England).
60. Albertson, R. (2004). Scribble protein domain mapping reveals a multistep localization mechanism and domains necessary for establishing cortical polarity. Journal of Cell Science.
61. Kukat, C., Wurm, C.A., Spahr, H., Falkenberg, M., Larsson, N.-G., and Jakobs, S. (2011). Super-resolution microscopy reveals that mammalian mitochondrial nucleoids have a uniform size and frequently contain a single copy of mtDNA. Proceedings of the National Academy of Sciences.
62. Xu, H., DeLuca, S.Z., and O'Farrell, P.H. (2008). Manipulating the metazoan mitochondrial genome with targeted restriction enzymes. Science.
63. Nakamura, K.C., Kameda, H., Koshimizu, Y., Yanagawa, Y., and Kaneko, T. (2008). Production and histological application of affinity-purified antibodies to heat-denatured green fluorescent protein. J Histochem Cytochem *56*, 647-657. 10.1369/jhc.2008.950915.
64. Diaz, F., Bayona-Bafaluy, M.P., Rana, M., Mora, M., Hao, H., and Moraes, C.T. (2002). Human mitochondrial DNA with large deletions repopulates organelles faster than full-length genomes under relaxed copy number control. Nucleic Acids Res *30*, 4626-4633. 10.1093/nar/gkf602.

65. Chiang, A.C.Y., Ježek, J., Mu, P., Di, Y., Klucnika, A., Jabůrek, M., Ježek, P., and Ma, H. (2024). Two mitochondrial DNA polymorphisms modulate cardiolipin binding and lead to synthetic lethality. Nat Commun *15*, 611. 10.1038/s41467-024-44964-2.
66. Matsuura, E.T., Chigusa, S.I., and Niki, Y. (1989). Induction of mitochondrial DNA heteroplasmy by intra- and interspecific transplantation of germ plasm in Drosophila. Genetics.
67. Chiang, A.C.Y., McCartney, E., O'Farrell, P.H., and Ma, H. (2019). A Genome-wide Screen Reveals that Reducing Mitochondrial DNA Polymerase Can Promote Elimination of Deleterious Mitochondrial Mutations. Current Biology.
68. Hill, J.H., Chen, Z., and Xu, H. (2014). Selective propagation of functional mitochondrial DNA during oogenesis restricts the transmission of a deleterious mitochondrial variant. Nature Genetics.
69. Palozzi, J.M., Jeedigunta, S.P., Minenkova, A.V., Monteiro, V.L., Thompson, Z.S., Lieber, T., and Hurd, T.R. (2022). Mitochondrial DNA quality control in the female germline requires a unique programmed mitophagy. Cell Metab *34*, 1809-1823.e1806. 10.1016/j.cmet.2022.10.005.
70. Zhang, Y., Wang, Z.-H., Liu, Y., Chen, Y., Sun, N., Gucek, M., Zhang, F., and Xu, H. (2019). PINK1 Inhibits Local Protein Synthesis to Limit Transmission of Deleterious Mitochondrial DNA Mutations. Molecular Cell.
71. Ma, H., Xu, H., and O'Farrell, P.H. (2014). Transmission of mitochondrial mutations and action of purifying selection in Drosophila melanogaster. Nature Genetics.
72. Chen, R., Grill, S., Lin, B., Saiduddin, M., and Lehmann, R. (2025). Origin and establishment of the germline in Drosophila melanogaster. Genetics *229*. 10.1093/genetics/iyae217.
73. Imbert, A., Ouyang, W., Safieddine, A., Coleno, E., Zimmer, C., Bertrand, E., Walter, T., and Mueller, F. (2022). FISH-quant v2: a scalable and modular tool for smFISH image analysis. Rna *28*, 786-795. 10.1261/rna.079073.121.
74. Zhang, Y., Chen, Y., Gucek, M., and Xu, H. (2016). The mitochondrial outer membrane protein MDI promotes local protein synthesis and mtDNA replication. The EMBO Journal.
75. Homem, C.C.F., and Knoblich, J.A. (2012). Drosophila neuroblasts: A model for stem cell biology. Development (Cambridge).
76. Albertson, R., Chabu, C., Sheehan, A., and Doe, C.Q. (2004). Scribble protein domain mapping reveals a multistep localization mechanism and domains necessary for establishing cortical polarity. J Cell Sci *117*, 6061-6070. 10.1242/jcs.01525.
77. Stewart, J.B., and Chinnery, P.F. (2015). The dynamics of mitochondrial DNA heteroplasmy: Implications for human health and disease. Nature Reviews Genetics.
78. Gorman, G.S., Chinnery, P.F., DiMauro, S., Hirano, M., Koga, Y., McFarland, R., Suomalainen, A., Thorburn, D.R., Zeviani, M., and Turnbull, D.M. (2016). Mitochondrial diseases. Nature Reviews Disease Primers. Nature Publishing Group.
79. Burgstaller, J.P., Kolbe, T., Havlicek, V., Hembach, S., Poulton, J., Piálek, J., Steinborn, R., Rülicke, T., Brem, G., Jones, N.S., and Johnston, I.G. (2018). Large-scale genetic analysis reveals mammalian mtDNA heteroplasmy dynamics and variance increase through lifetimes and generations. Nature Communications *9*, 2488. 10.1038/s41467-018-04797-2.
80. Johnston, I.G., Burgstaller, J.P., Havlicek, V., Kolbe, T., Rülicke, T., Brem, G., Poulton, J., and Jones, N.S. (2015). Stochastic modelling, Bayesian inference, and new in vivo measurements elucidate the debated mtDNA bottleneck mechanism. eLife *4*, e07464. 10.7554/eLife.07464.
81. Soong, N.W., Hinton, D.R., Cortopassi, G., and Arnheim, N. (1992). Mosaicism for a specific somatic mitochondrial DNA mutation in adult human brain. Nature Genetics.

82. Kosanke, M., Davenport, C., Szepes, M., Wiehlmann, L., Kohrn, T., Dorda, M., Gruber, J., Menge, K., Sievert, M., Melchert, A., et al. (2021). iPSC culture expansion selects against putatively actionable mutations in the mitochondrial genome. Stem Cell Reports *16*, 2488-2502. 10.1016/j.stemcr.2021.08.016.
83. Aryaman, J., Bowles, C., Jones, N.S., and Johnston, I.G. (2019). Mitochondrial Network State Scales mtDNA Genetic Dynamics. Genetics *212*, 1429-1443. 10.1534/genetics.119.302423.
84. Edwards, D.M., Røyrvik, E.C., Chustecki, J.M., Giannakis, K., Glastad, R.C., Radzvilavicius, A.L., and Johnston, I.G. (2021). Avoiding organelle mutational meltdown across eukaryotes with or without a germline bottleneck. PLoS Biol *19*, e3001153. 10.1371/journal.pbio.3001153.
85. Ahier, A., Dai, C.Y., Kirmes, I., Cummins, N., Hung, G.C.C., Götz, J., and Zuryn, S. (2021). PINK1 and parkin shape the organism-wide distribution of a deleterious mitochondrial genome. Cell Rep *35*, 109203. 10.1016/j.celrep.2021.109203.
86. Bess, A.S., Crocker, T.L., Ryde, I.T., and Meyer, J.N. (2012). Mitochondrial dynamics and autophagy aid in removal of persistent mitochondrial DNA damage in Caenorhabditis elegans. Nucleic Acids Research.
87. Suen, D.-F., Narendra, D.P., Tanaka, A., Manfredi, G., and Youle, R.J. (2010). Parkin overexpression selects against a deleterious mtDNA mutation in heteroplasmic cybrid cells. Proceedings of the National Academy of Sciences.
88. Katajisto, P., Döhla, J., Chaffer, C.L., Pentinmikko, N., Marjanovic, N., Iqbal, S., Zoncu, R., Chen, W., Weinberg, R.A., and Sabatini, D.M. (2015). Asymmetric apportioning of aged mitochondria between daughter cells is required for stemness. Science.
89. Raap, A.K., Jahangir Tafrechi, R.S., van de Rijke, F.M., Pyle, A., Wählby, C., Szuhai, K., Ravelli, R.B., de Coo, R.F., Rajasimha, H.K., Nilsson, M., et al. (2012). Non-random mtDNA segregation patterns indicate a metastable heteroplasmic segregation unit in m.3243A>G cybrid cells. PLoS One *7*, e52080. 10.1371/journal.pone.0052080.
90. McFaline-Figueroa, J.R., Vevea, J., Swayne, T.C., Zhou, C., Liu, C., Leung, G., Boldogh, I.R., and Pon, L.A. (2011). Mitochondrial quality control during inheritance is associated with lifespan and mother-daughter age asymmetry in budding yeast. Aging Cell.
91. Vevea, J.D., Swayne, T.C., Boldogh, I.R., and Pon, L.A. (2014). Inheritance of the fittest mitochondria in yeast. Trends Cell Biol *24*, 53-60. 10.1016/j.tcb.2013.07.003.
92. Dua, N., Seshadri, A., and Badrinarayanan, A. (2022). DarT-mediated mtDNA damage induces dynamic reorganization and selective segregation of mitochondria. J Cell Biol *221*. 10.1083/jcb.202205104.
93. Horvitz, H.R., and Herskowitz, I. (1992). Mechanisms of asymmetric cell division: Two Bs or not two Bs, that is the question. Cell *68*, 237-255. https://doi.org/10.1016/0092-8674(92)90468-R.
94. Sen, A., Boix, J., and Pla-Martín, D. (2023). Endosomal-dependent mitophagy coordinates mitochondrial nucleoid and mtDNA elimination. Autophagy *19*, 2609-2610. 10.1080/15548627.2023.2170959.
95. Liu, H., Zhen, C., Xie, J., Luo, Z., Zeng, L., Zhao, G., Lu, S., Zhuang, H., Fan, H., Li, X., et al. (2024). TFAM is an autophagy receptor that limits inflammation by binding to cytoplasmic mitochondrial DNA. Nat Cell Biol *26*, 878-891. 10.1038/s41556-024-01419-6.
96. Tábara, L.C., Burr, S.P., Frison, M., Chowdhury, S.R., Paupe, V., Nie, Y., Johnson, M., Villar-Azpillaga, J., Viegas, F., Segawa, M., et al. (2024). MTFP1 controls mitochondrial fusion to regulate inner membrane quality control and maintain mtDNA levels. Cell *187*, 3619-3637.e3627. 10.1016/j.cell.2024.05.017.
97. Kondo, T., Asai, M., Tsukita, K., Kutoku, Y., Ohsawa, Y., Sunada, Y., Imamura, K., Egawa, N., Yahata, N., Okita, K., et al. (2013). Modeling Alzheimer's disease with iPSCs reveals stress

phenotypes associated with intracellular Abeta and differential drug responsiveness. Cell Stem Cell. 2013/02/26 ed.
98. Begeman, A., Smolka, J.A., Shami, A., Waingankar, T.P., and Lewis, S.C. (2025). Spatial analysis of mitochondrial gene expression reveals dynamic translation hubs and remodeling in stress. Sci Adv *11*, eads6830. 10.1126/sciadv.ads6830.
99. Harzer, H., Berger, C., Conder, R., Schmauss, G., and Knoblich, J.A. (2013). FACS purification of Drosophila larval neuroblasts for next-generation sequencing. Nature Protocols.
100. Burr, S.P., and Chinnery, P.F. (2022). Measuring Single-Cell Mitochondrial DNA Copy Number and Heteroplasmy using Digital Droplet Polymerase Chain Reaction. J Vis Exp. 10.3791/63870.
101. Nash, P.A., Silva-Pinheiro, P., and Minczuk, M.A. (2023). Genotyping Single Nucleotide Polymorphisms in the Mitochondrial Genome by Pyrosequencing. J Vis Exp. 10.3791/64361.
102. Andréasson, H., Asp, A., Alderborn, A., Gyllensten, U., and Allen, M. (2002). Mitochondrial sequence analysis for forensic identification using pyrosequencing technology. Biotechniques *32*, 124-126, 128, 130-123. 10.2144/02321rr01.
103. Loyer, N., and Januschke, J. (2018). The last-born daughter cell contributes to division orientation of Drosophila larval neuroblasts. Nature Communications *9*, 3745. 10.1038/s41467-018-06276-0.
104. Legland, D., Arganda-Carreras, I., and Andrey, P. (2016). MorphoLibJ: integrated library and plugins for mathematical morphology with ImageJ. Bioinformatics *32*, 3532-3534. 10.1093/bioinformatics/btw413.
105. Mueller, F., Senecal, A., Tantale, K., Marie-Nelly, H., Ly, N., Collin, O., Basyuk, E., Bertrand, E., Darzacq, X., and Zimmer, C. (2013). FISH-quant: automatic counting of transcripts in 3D FISH images. Nat Methods *10*, 277-278. 10.1038/nmeth.2406.
106. Schindelin, J., Arganda-Carreras, I., Frise, E., Kaynig, V., Longair, M., Pietzsch, T., Preibisch, S., Rueden, C., Saalfeld, S., Schmid, B., et al. (2012). Fiji: an open-source platform for biological-image analysis. Nat Methods *9*, 676-682. 10.1038/nmeth.2019.
107. Rueden, C.T., Schindelin, J., Hiner, M.C., DeZonia, B.E., Walter, A.E., Arena, E.T., and Eliceiri, K.W. (2017). ImageJ2: ImageJ for the next generation of scientific image data. BMC Bioinformatics *18*, 529. 10.1186/s12859-017-1934-z.
108. R Core Team (2021). R: A Language and Environment for Statistical Computing. https://www.R-project.org/.
109. Pinheiro, J., Bates, D., and Team}, R.C. (2025). nlme: Linear and Nonlinear Mixed Effects Models.
110. Wonnapinij, P., Chinnery, P.F., and Samuels, D.C. (2010). Previous estimates of mitochondrial DNA mutation level variance did not account for sampling error: comparing the mtDNA genetic bottleneck in mice and humans. Am J Hum Genet *86*, 540-550. 10.1016/j.ajhg.2010.02.023.
111. Johnston, I.G., and Jones, N.S. (2016). Evolution of Cell-to-Cell Variability in Stochastic, Controlled, Heteroplasmic mtDNA Populations. Am J Hum Genet *99*, 1150-1162. 10.1016/j.ajhg.2016.09.016.
112. Pudlo, P., Marin, J.-M., Estoup, A., Cornuet, J.-M., Gautier, M., and Robert, C.P. (2015). Reliable ABC model choice via random forests. Bioinformatics *32*, 859-866. 10.1093/bioinformatics/btv684.
113. Lenormand, M., Jabot, F., and Deffuant, G. (2013). Adaptive approximate Bayesian computation for complex models. Computational Statistics *28*, 2777-2796. 10.1007/s00180-013-0428-3.

114. Jabot, F., Faure, T., and Dumoulin, N. (2013). EasyABC: performing efficient approximate Bayesian computation sampling schemes using R. Methods in Ecology and Evolution *4*, 684-687. https://doi.org/10.1111/2041-210X.12050.